Scalable Photovoltaic-Electrochemical Cells for Hydrogen Production from Water - Recent Advances
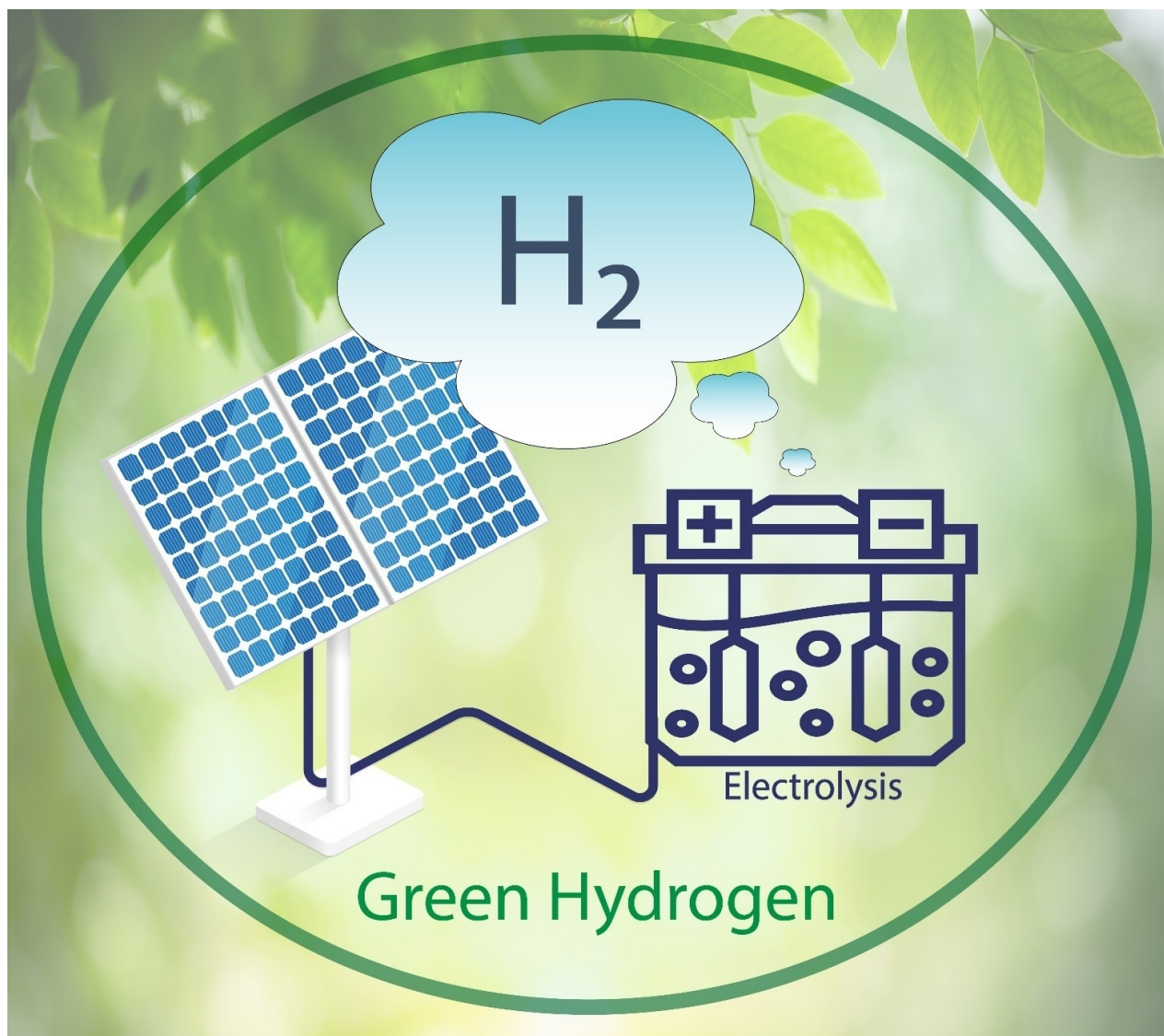
Minoh Lee,*[a] Stefan Haas,[a] Vladimir Smirnov,[a] Tsvetelina Merdzhanova,[a] and Uwe Rau[a, b]

ChemElectroChem

Review
doi.org/10.1002/celc.202200838

Chemistry Europe
European Chemical
Societies Publishing

Hydrogen is regarded as a very important pillar for the future energy supply because it is readily available from water and can be used for environmentally friendly electricity generation. Hydrogen can be produced in various ways. Water splitting powered by renewable resources (e.g., solar, wind, etc.) can be an ideal way of hydrogen generation in the future since this approach can achieve true net-zero carbon dioxide emissions. This review article is aimed at giving an overview of the state-of-the-art hydrogen generation driven by photovoltaics (PVs) on a relatively large-scale (with PV area >50 cm^2). The basic knowledge/principle of (PV-driven) water splitting is introduced in the beginning part. Then, different types of PV-driven water splitting devices and the recent advances in scalable PV-electrochemical water splitting devices are intensively reviewed in the middle part. Finally, cost predictions and challenges that need to be addressed are presented at the end of this article.

1. Introduction

Even though fossil fuels (e.g., coal, petroleum, and natural gas) have enriched our lives for a long time, we are now facing severe challenges associated with global warming, air pollution, and depletion of fossil fuels.[1] To cope with climate change, 195 states set out international goals in Paris in 2015, where the average temperature increase should be limited to below 2 °C.[2] In an effort to reduce the use of fossil fuels, interests in renewable and net-zero carbon footprint energy sources (e.g., sunlight, wind, biomass, waves, tides, etc.) have been significantly increasing.[3] Solar energy can provide 23,000 TW per year, which is dominant among renewable energy sources.[4] While solar energy can be converted into electricity by employing the most commonly used solar cells (or photovoltaic cells; hereafter we use PV as an abbreviation of photovoltaic), the intermittency of solar energy caused by the cycles of nature has remained of primary importance to the sustainable energy supply.[5] To overcome such a drawback, many researchers have been trying to convert solar energy into a form of chemical compound that is generated when the sun shines and can be used upon demand.[6] The research concerning storing solar energy in the form of hydrogen has been centered in the field of solar fuel since hydrogen is one of the most promising future energy carriers.[7] At present, most of the hydrogen (95%) is produced by a system (grey hydrogen) that reforms, especially the less heavy hydrocarbons (methane reforming).[8] Although this process is highly efficient in generating hydrogen, a harsh combustion process is required. High quantities of CO_2 can be a concomitant of the reforming process resulting in global warming.[9] Electrolysis, which is a process of water decomposition into oxygen and hydrogen, has been getting a lot of attention as one of the alternatives because any environmentally harmful by-products are not generated in such a process. If electrolysis is induced by solar energy, such a solar-driven hydrogen process can be a perfect platform for storing energy in a more sustainable foam and simultaneously achieving net-zero carbon dioxide emissions.[8,9b]

In the current review article, we cover PV-driven water splitting among the three different concepts of solar water splitting approaches (i.e., PC: particulate,[10] PEC: photoelectrochemical,[11] PV-EC: PV-electrochemical[7a]). Although PV-based water splitting technology makes the device body more complexly structured leading to more expensive than other concepts, this system was already partially commercialized with a high solar-to-hydrogen (STH) efficiency of 10% and can be a dominant approach for a market release in the short term (<10 years) since PV-EC technology is well matured compared to PC and PEC.[12] Improving the overall efficiencies and stability of both PV and EC should be considered first to prepare the PV-EC system for market release. Additionally, the fabrication of a device at a large-scale would be an essential prerequisite for launching onto the market.[7a]

Here, we mainly focus on the recent advances in the upscaled (with PV area >50 cm^2) PV-EC water splitting device. First, we provide the fundamental aspects of (solar) electrochemical water splitting and then introduce concepts of three different solar water splitting devices. In the middle part, the working principle and different structures of PV-EC devices are described, followed by state-of-the-art upscaled PV-EC technologies, which are intensively reviewed and discussed. Finally, a summary of this review article, perspective, and challenges the community should address in the near future is presented.

2. Photovoltaic-Electrochemical Cells for Hydrogen Production

2.1. Basics of water splitting

The overall water electrolysis involves two half-cell reactions that are water reduction reaction (hydrogen evolution reaction: HER) and water oxidation reaction (oxygen evolution reaction: OER). The cathodic (HER: Equations 1 and 3) and anodic (OER: Equations 2 and 4) equations can be expressed depending on the electrolyte conditions (pH value in solution) in the following manner where SHE indicates the standard hydrogen electrode.[7b,13]
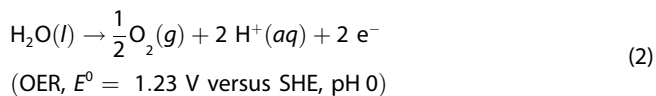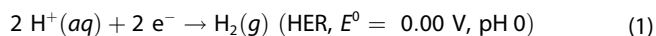
[a] Dr. M. Lee, Dr. S. Haas, Dr. V. Smirnov, Dr. T. Merdzhanova, Prof. U. Rau
Institut für Energie- und Klimaforschung (IEK-5)
Forschungszentrum Jülich GmbH
52428 Jülich, Germany
E-mail: molee0422@gmail.com
[b] Prof. U. Rau
Faculty of Electrical Engineering and Information Technology
RWTH Aachen University
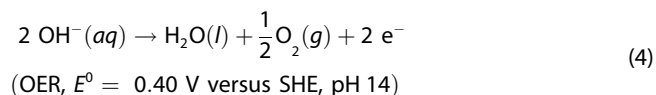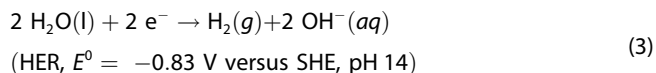Mies-van-der-Rohe-Straße 15, 52074 Aachen, Germany

Supporting information for this article is available on the WWW under https://doi.org/10.1002/celc.202200838

ChemElectroChem

Review
doi.org/10.1002/celc.202200838

Chemistry
Europe
European Chemical
Societies Publishing

In acid (pH 0),

$$2\,H^+(aq) + 2\,e^- \rightarrow H_2(g) \quad (HER,\, E^0 = 0.00\,V,\, pH\,0) \tag{1}$$

$$H_2O(l) \rightarrow \frac{1}{2}O_2(g) + 2\,H^+(aq) + 2\,e^-$$
$$(OER,\, E^0 = 1.23\,V\text{ versus SHE, pH 0}) \tag{2}$$

In alkaline (pH 14),

$$2\,H_2O(l) + 2\,e^- \rightarrow H_2(g) + 2\,OH^-(aq)$$
$$(HER,\, E^0 = -0.83\,V\text{ versus SHE, pH 14}) \tag{3}$$

$$2\,OH^-(aq) \rightarrow H_2O(l) + \frac{1}{2}O_2(g) + 2\,e^-$$
$$(OER,\, E^0 = 0.40\,V\text{ versus SHE, pH 14}) \tag{4}$$

Thereby, total reaction can be written by Equation 5

$$H_2O(l) \rightarrow H_2(g) + \frac{1}{2}O_2(g) \quad (\Delta E = 1.23\,V) \tag{5}$$
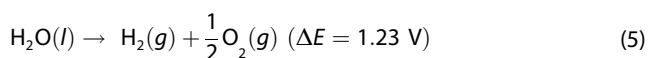
External electricity input of the change in Gibbs free energy $\Delta G^0 = -n\,F\,E^0 = \sim 237\,kJ\,mol^{-1}$ is required to split water (liquid) into H_2 gas and O_2 gas. Where n_e is the number of electrons ($n = 2$), F is Faraday constant ($F = 96,485.3321233\,C\,mol^{-1}$) and E^0 is the thermodynamic standard cell potential ($E^0 = -1.229\,V$). The detailed reaction routes of HER and OER are schematically shown in Figure 1a. Notably, here the way in acid is only shown for a better fundamental understanding. In the case of HER (in acid medium), the reduction of a proton (H^+)/or hydronium ions (H_3O^+) takes place on the active sites of the catalyst at the beginning step. This process is called as Vomer step. Followed by hydrogen gas can be evolved via either a consecutive reduction of the proton (H^+)/or hydronium ions (H_3O^+) together with electron transfer (Tafel step) or the recombination of two adsorbed protons placed adjacent to

each other (Heyrovsky step).[14] When the HER takes place in an alkaline electrolyte, the water molecule is reduced on the active site of the catalysts at the beginning step. Thereby proton is formed at the active site of the catalysts. That's why more energy (i.e., overpotential) than acid media is mostly required to generate protons by breaking water molecules.[13b] In contrast to the HER, a four-electron transfer process is required to generate 1 M of O_2 gas. Thus, OER is considered a bottleneck process in the whole water electrolysis system. Even though four different types of reaction mechanisms of OER have been suggested,[15] here, the most recognized two mechanisms electrochemical oxide, and oxide pathways, are only included in Figure 1a. As the first step, a water molecule is dissociated with the release of a proton, and then, hydroxide is adsorbed on the catalyst's active site. Followed by an oxygen bond can be generated through either a successive proton release (electrochemical oxidation) or oxidation along with the release of a water molecule. Thereby, two adsorbed oxygen atoms can result in the evolution of O_2. For the OER mechanism in alkaline media, the hydroxide ion is adsorbed on the catalyst's active site at the beginning step. And then, either a radical oxo coupling path or superoxo intermediate path can be possible for the evolution of O_2.[16] Further detailed mechanisms of electrochemical water splitting can be found in the articles.[13,16,18] Although water electrolysis is efficient and well-studied in electrolytes with a high ionic concentration, H_2 needs to be generated from pure water or equivalent electrolytes for commercial viability and sustainability.

2.2. Different concepts of solar water splitting devices

Solar energy-driven H_2 production systems can be roughly divided into three different concepts that are I) particulate photocatalyst (PC), II) photoelectrochemical (PEC), and III) photovoltaic-electrochemical (PV-EC) systems, which are schematically described in Figure 2a–c. In the case of the particulate

Minoh Lee is currently working as a research professor at Korea University. From 2016 to 2022 he worked at Korea Institute of Science and Technology (South Korea), Forschungzentrum Juelich (Germany), and University of Toronto (Canada). He received Ph.D. degree in 2016 from Ulsan National Institute of Science and Technology (South Korea). His research interests are centered on photoelectrochemical energy conversion (solar fuels), solar cells, and heterogeneous electrocatalysts for the production of fuels.

Vladimir Smirnov received his Ph.D. degree in 2006 (Dundee, United Kingdom) and since 2007 he is a scientist at the Institute of Energy and Climate Research 5 (IEK-5), Forschungszentrum Jülich, Germany. His research interests are focused on developing materials and devices for solar energy conversion and solar fuels. Current efforts focus on high efficiency solar cells, integrated photo-electrochemical devices and device upscaling.

Tsvetelina Merdzhanova received her Ph.D. degree in physics in 2005. After that she joined the MPI for Solid State Research in Stuttgart as a post-doc. Since 2013 became a leader of the Photovoltaic-electrochemical devices group at IEK-5 Photovoltaik, Forschungzentrum Juelich (FZJ) with focus on silicon solar cells and modules for PV-storage system integration.
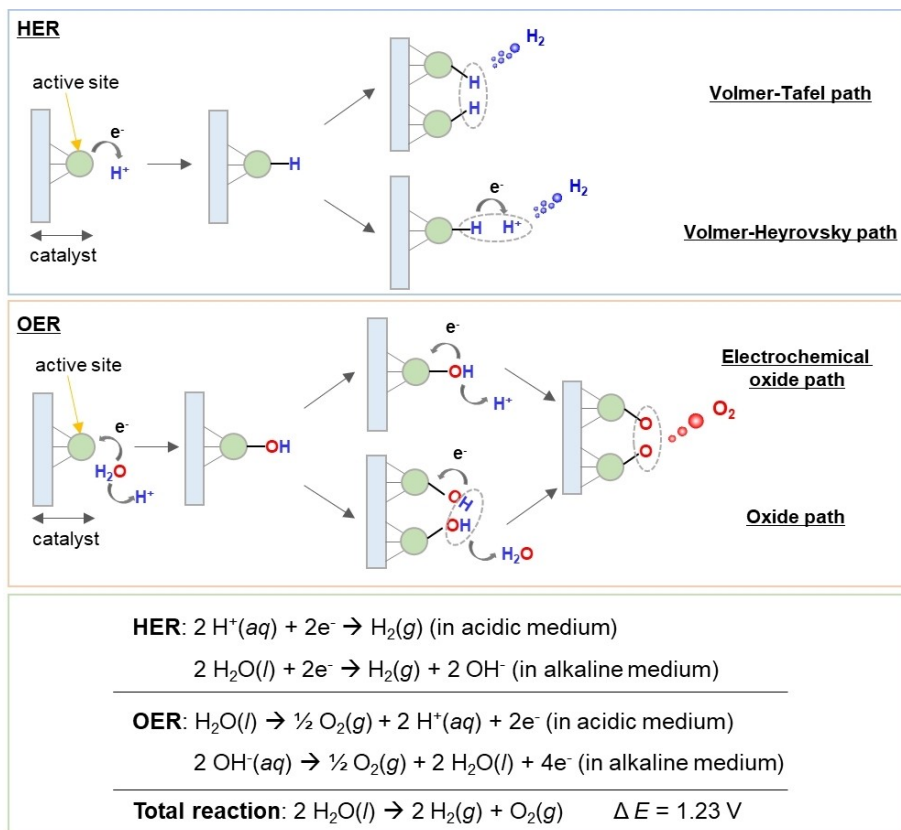
Figure 1. Prevailing mechanism of electrochemical water splitting reactions. Schematic images represent a water splitting reaction in an acidic aqueous solution. HER and OER indicate hydrogen evolution reaction and oxygen evolution reaction, respectively.

PC system, as shown in Figure 2a, semiconductor particles shown with light orange-colored circles are dispersed in the electrolyte. The particulate PC system has the advantage of simplicity in that it only consists of a semiconductor (or catalysts can be decorated on the surface PC for an efficient system). Thus, the total system can be made inexpensively.[10,17,19] Despite the cost advantage, the value of a STH efficiency for spontaneous overall water splitting remains at around 1%.[19a,20] Other factors also must be considered, such as the suitable band position of semiconductors, chemical stability against corrosion, and dispersion stability of semiconductor powders to establish an efficient and stable system. More detailed information about particulate PC water splitting systems can be found in recent review articles.[19a]

As shown in Figure 2b, photoelectrodes (i.e., n-type semiconductor as a photoanode, p-type semiconductor as a photocathode) are immersed in the electrolyte in a PEC system. Notably, a combination of n- and p-doped semiconductors systems is shown for spontaneous overall water splitting. In contrast to the particulate PC system, metallic substrates are used as charge collectors. Additionally, generated H_2 and O_2 gases can be separated in a PEC system by placing a membrane, avoiding a gas explosion and the efficiency loss caused by the back reactions (i.e., hydrogen oxidation and oxygen reduction reactions).[21] Band bending at the semiconductor-liquid junction (as an indicator of driving force for

charge separation) is more apparent than that of a particulate PC system, which results in a more efficient system.[7a] While a PEC system has shown promising properties for H_2 production, there are still challenges associated with chemical stability (i.e., corrosion against electrolyte) and slow charge transfer at the semiconductor-liquid interface. A lot of efforts have been made to address these issues by introducing passivation layers and electrocatalysts on the surface of semiconductors. Extensive insights into the field of PEC systems can be found in review articles.[11,22]

Coupling a PV module to an electrolyzer (Figure 2c) is one of the viable paths for solar H_2 production. In this case, PV and catalysts (here OER and HER electrocatalysts) are electrically connected by a conductive wire. The electricity generated by PV independently can be transferred to the EC part. Notably, the photovoltage of PV cells is required above ~1.6 V (considering overpotential losses of HER and OER, and trade-off of current and voltage in PV) for the spontaneous overall water splitting. Thus, either a module (or cells) consisting of a laterally series-connected structure or a vertically integrated multi-junction structure should be considered a power source.[23] Compared with the particulate PC and the PEC approaches, less of a concern about the chemical stability can be needed in a PV-EC system since a photoabsorber where electron-hole pair is generated can be positioned outside of an electrolyzer (also gases separation can be possible in an electrolyzer). It should
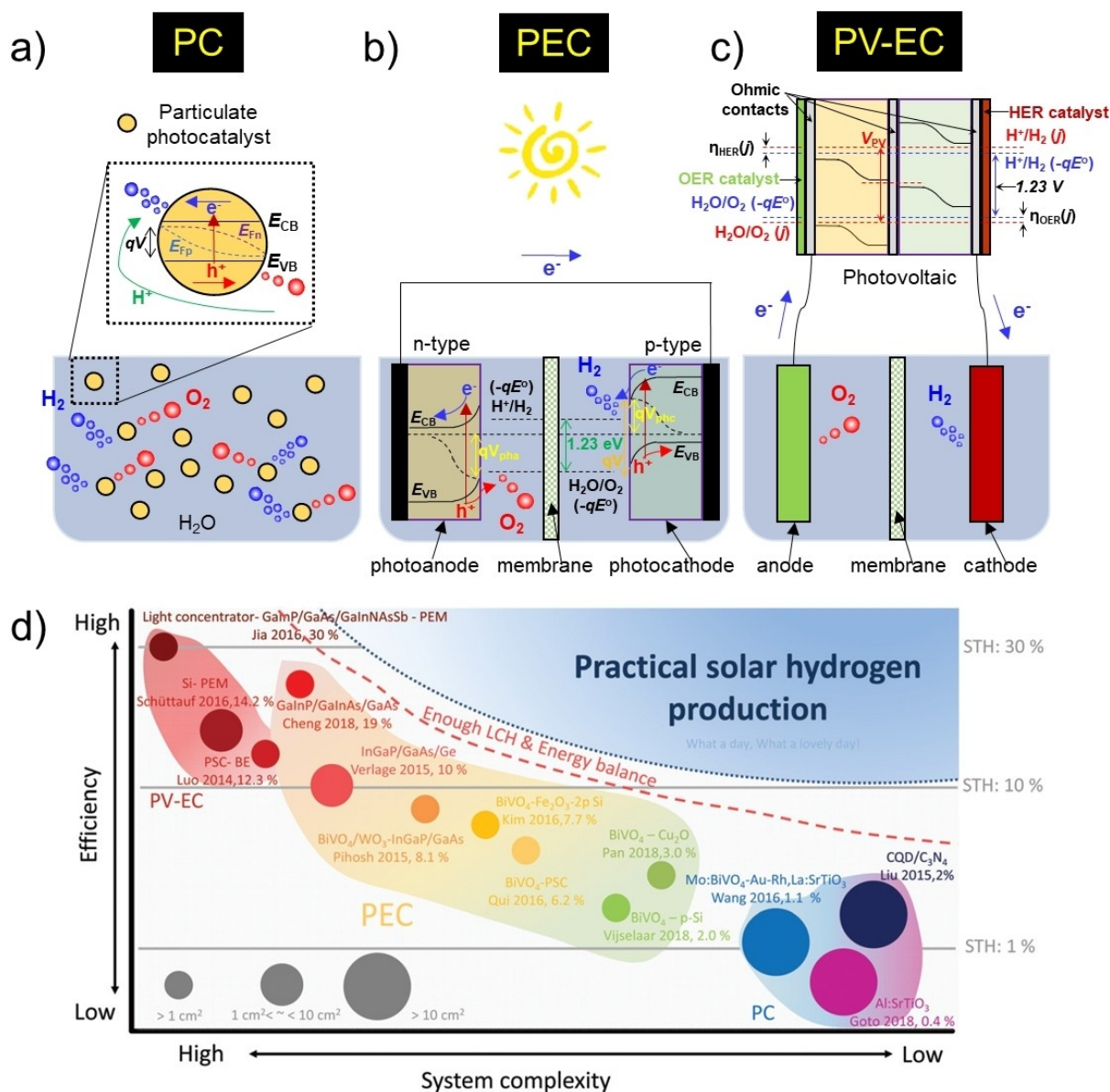
ChemElectroChem

Review
doi.org/10.1002/celc.202200838

Chemistry
Europe
European Chemical
Societies Publishing

Figure 2. Three different types of water splitting systems; (a) particulate photocatalyst (PC), (b) photoelectrochemical (PEC), (c) photovoltaic-electrochemical (PV-EC) approaches. Where energy scale stands for conduction band energy (E_{CB}), valance band energy (E_{VB}), quasi-Fermi level for electrons (E_{Fn}) and holes (E_{Fp}) upon excitation by solar energy, n-doped semiconductor (n-type), p-doped semiconductor (p-type), photovoltage for photoanode (qV_{pha}) and photocathode (qV_{phc}), the voltage of PV (V_{PV}), the electrochemical thermodynamic potentials of both proton reduction [H^+/H_2 ($-qE^o$)] and water oxidation [$-qE^o(O_2/H_2O)$], electrochemical potentials of both proton reduction H^+/H_2 (j) and water oxidation H_2O/O_2 (j) in coupled PV-EC device, and overpotentials of HER [$\eta_{HER}(j)$] and OER [$\eta_{OER}(j)$]. Reproduced from Ref. [26] Copyright (2012), with permission from United States National Academy of Sciences. (d) Technological map of solar water splitting systems. 13 experimental demonstrations are shown with colorful circles, and each approach has distinct advantages and disadvantages. Reproduced from Ref. [7a, 27] Copyright (2019, 2014), with permission from Royal Society of Chemistry, National Institute of Advanced Industrial Science and Technology.

be pointed out, even though the concept here shows that PV is positioned out of an electrolyzer, PV can also be located in the electrolyte (see Figures 4, 6, 8 and 10). Although the preparation of a PV-EC system is more complicated than the other particulate PC and PEC systems, a PV-EC system holds high levels of STH efficiencies (see Figure 2d). Also, both PV and electrolyzer systems are already well matured.[24] Additionally, the cost of each part of PV and electrolyzer has been continuously decreasing, making a PV-EC system more competitive in the supply of eco-friendly and sustainable H_2.[8,25]

2.3. Principle of PV-powered water splitting

The block diagram of an integrated PV-EC system is given in Figure 3a. When the PV is coupled with EC, the electrical output (J_{PV} and V_{PV}) of the PV becomes equivalent to the electrical input of the EC part ($J_{PV} = J_{EC}$ and $V_{PV} = V_{EC}$).

The equivalent circuit of the integrated PV-EC system is shown in Figure 3b. Precise modeling of PV-EC integrated systems can be enabled by circuit analysis, which can be a practical experimental guide predicting how well the PV-EC
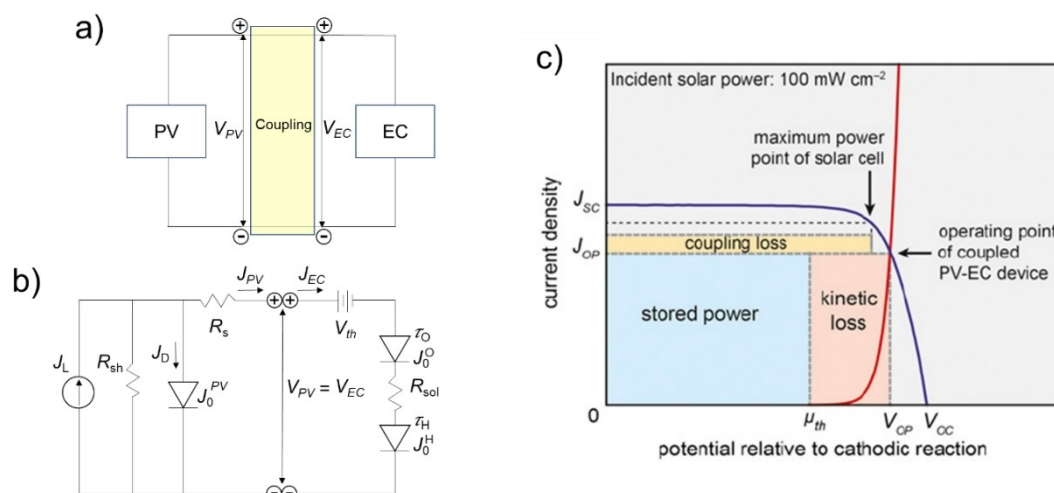
ChemElectroChem

Review
doi.org/10.1002/celc.202200838

Chemistry
Europe
European Chemical
Societies Publishing

Figure 3. (a) Block diagram of directly coupled PV and EC for water splitting and (b) corresponding steady-state equivalent circuit of an integrated PV-EC system. (c) The diagram of the PV-EC system is coupled through a direct electrical connection. The power flows are graphically identified in a graph, and the current density-voltage (*J-V*) curves of PV (blue line) and EC (red line) are shown. The intersection of each *J-V* curve is considered the operation current of the PV-EC system. V_{oc} is open-circuit voltage, J_{sc} is short-circuit current density, J_{op} is operating current density, V_{op} is operating voltage, μ_{th} is thermodynamic reaction potential. Reproduced from Ref. [28] Copyright (2013), with permission from United States National Academy of Sciences.
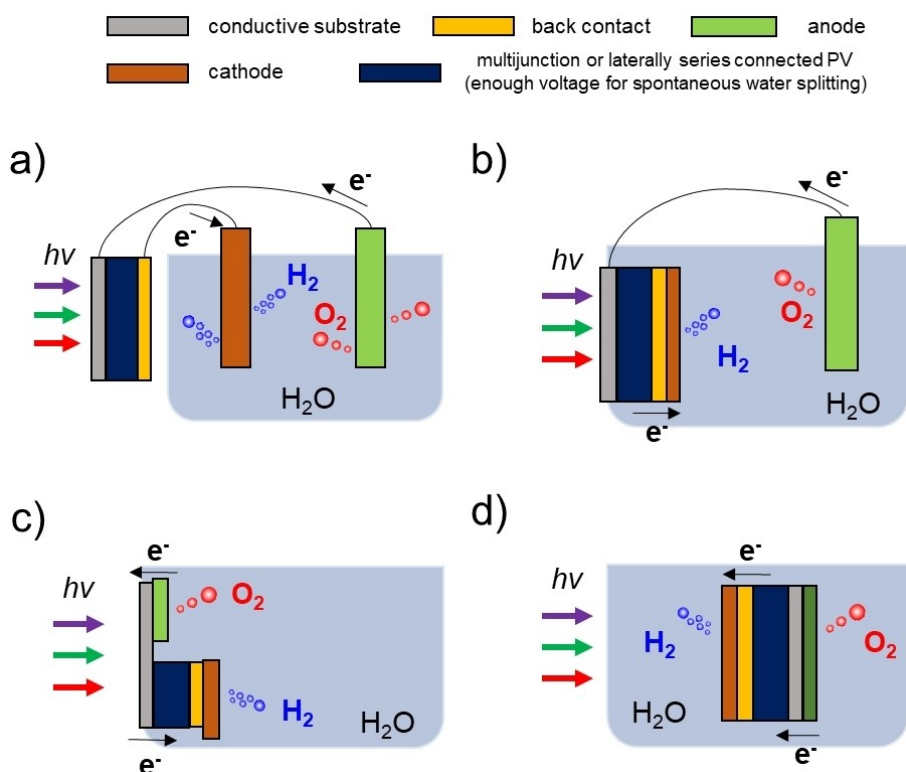

Figure 4. Four different categories of unbiased PV-driven water splitting devices. (a) PV is directly connected to an electrolyzer; this type is most widely used in the field of unbiased PV-driven water splitting. Combined with DC/DC converters, this concept has already been commercialized. One of the representatives in Ref. [32c]. (b) A combination of PV with opposing photoanode (or photocathode) and HER cathode (or OER anode). One of the representatives in Ref. [41] (c) Wireless design with the side-by-side arrangement of HER and OER. One of the representatives in Ref. [42]. (d) Wireless design with PV part is embedded between the catalysts. One of the representatives in Ref. [43]

integrated system operates and the efficiency limitation. Each decoupled PV and EC model system can be expressed as follows.[28] Note that all equations below in this section would be suitable for one of the configurations (Figure 4.1, Section 2.6), but might not be universal for all cases.

$$PV : J_{PV} = J_L - J_0 \exp\left(\frac{V_{PV} + J_{PV}R_S}{nV_{th}}\right) - \left(\frac{V_{PV} + J_{PV}R_S}{R_{sh}}\right) \quad (6)$$

$$EC : V_{EC} = \mu_{th} + \tau_{OER}\log\left(\frac{J_{EC}}{J_0^{OER}}\right) +$$

$$\tau_{HER}\log\left(\frac{J_{EC}}{J_0^{HER}}\right) + J_{EC}R_{Sol} \quad (7)$$

Equation 6 indicates the diode equation of the PV system, where the output current density J_{PV} is defined as the difference between the generated current by light illumination J_L and the recombination currents (diode current + shunt current). Where dark saturation current density is J_0, operating voltage is V_{PV}, n is diode ideality factor, thermal voltage is V_{th} that is equal to k_bT/q (q is the electron charge, T is temperature, and k_b is Boltzmann constant), R_s is series resistance, and R_{sh} is shunt resistance.

Equation 7 indicates the J-V relationship of EC. The total potential in the EC system (V_{EC}) can be divided into four parts. Thermodynamic potential μ_{th} (here 1.23 V for water splitting) implies an ideal case where the reaction occurs, voltage losses (overpotential) at OER and HER electrodes, and electrolyte [multiplication of a current (J_{EC}) and a solution resistance (R_{sol}) in EC system]. Therefore, the operating voltage V_{op} is required to exceed μ_{th} (1.23 V) to generate fuel (here hydrogen) in the real system. The Tafel slope and the exchange current density can be represented with the terms of τ and J_0, respectively. The Tafel slope means the potential change per decade of current (mV dec^{-1}), which can generally be (in case of sufficiently large overpotentials, here we are not dealing in detail, see the Butler-Volmer expression and equation deployment of J–V relationship of EC[29] expressed with $\tau = RT/\alpha n_cF$ where R is ideal constant, α is transfer coefficient, n_c is a number of charge carriers, and F is faradaic constant. The exchange current density describes the rate of oxidation and reduction at an equilibrium electrode.

In the integrated PV-EC arrangement, the total solar to fuel conversion efficiency (η_{SF}) comprises three efficiency terms (Equation 8).

$$\eta_{SF} = \eta_{PV} \times \eta_{EC} \times \eta_C \quad (8)$$

Where η_{PV} is solar to electricity the conversion efficiency of PV, η_{EC} is the efficiency of the EC system and η_C is the coupling efficiency between PV and EC.

Each representing parameter is graphically explained in Figure 3c.

Equation 9 indicates η_{PV} has defined the ratio of the converted electricity to the given solar irradiance P_{sun}, which can be denoted with PV parameters (fill factor $FF = J_{mp}V_{mp}/J_{sc}V_{oc}$, open-circuit voltage V_{oc}, short circuit current J_{sc}). Where J_{mp} and V_{mp} indicate current density and voltage at the maximum point, respectively.

$$\eta_{PV} = \frac{FF \times V_{oc} \times J_{sc}}{P_{sun}} \quad (9)$$

In the case of η_{EC} (Equation 10), kinetic limitations are generally considered a dominant factor rather than thermodynamic ones. The η_{EC} can be described with a ratio of the stored hydrogen power $\mu_{th}J_{op}$ to the total electrical energy $V_{op}J_{op}$ as follows.

$$\eta_{EC} = \frac{\mu_{th} \times J_{op}}{V_{op} \times J_{op}} = \frac{\mu_{th}}{V_{op}} \quad (10)$$

Equation 11 indicates The operation state of the integrated PV-EC system can be determined at the crossing point of the individual I–V curves of PV and EC. The last determining efficiency term η_C can be expressed with a ratio of the operation power to its maximum output.

$$\eta_C = \frac{V_{op} \times J_{op}}{V_{mp} \times J_{mp}} = \frac{V_{op} \times J_{op}}{FF \times V_{oc} \times J_{sc}} \quad (11)$$

Therefore, the η_{SF} can be simplified by combining the above three key efficiency expressions as follows.

$$\eta_{SF} = \frac{FF \times V_{oc} \times J_{sc}}{P_{sun}} \times \frac{\mu_{th}}{V_{op}} \times \frac{V_{op} \times J_{op}}{FF \times V_{oc} \times J_{sc}} = \frac{\mu_{th} \ (1.23 \ V) \times J_{op}}{P_{sun}} \quad (12)$$

As shown in the last term in Equation 12, the solar fuel efficiency can be calculated by the operation current in the integrated PV-EC device per solar power unit. Here the thermodynamic potential of reactions (here water splitting 1.23 V) is constant. Notably, this equation assumes 100% of the faradaic efficiency of product generation.

Since J_{PV} is equal to J_{EC} in the integrated PV-EC device, the crossing point where both I–V curves meet can ideally be considered operation current J_{op} [the maximum STH efficiency can be predicted by the 'reverse analysis' where the polarization curves of EC can be considered for the maximum STH efficiency by coupling to the maximum power point (MPP) of PV devices].[6m] Consequently, many articles report solar fuel efficiency by using the crossing point as operation current. Although we can predict the realistic performance with this crossing point, real operation current cannot be entirely compatible with the expected value since the respective I–V curves of PV and EC are affected by scan rate and sweep direction. Additionally, during the I–V measurement, characteristics/or structure/or morphology (due to the voltage-dependent migration, redox reactions/capacitance current, dissolution, etc.) can be changed in each PV and EC. Therefore, steady-state measurement of operation current (or bubbles) should be accompanied to show more reliable results.

With each I–V curve of PV and EC, we can also estimate the stored power (here H$_2$), kinetic loss, and coupling loss. The stored hydrogen power (P$_{H2}$) is proportional to the operation current (crossing point). Therefore, to obtain a higher P$_{H2}$, the crossing point needs to be positioned close to the J_{sc}. However, in this case, the operating power of PV-EC (P$_{H2}$ + P$_{KIN}$) cannot be exceeding the maximum power (@PV$_{mp}$), and coupling loss can be minimized by introducing dc/dc converter that can enable tracking the correct maximum power point in the integrated

ChemElectroChem

Review
doi.org/10.1002/celc.202200838

Chemistry Europe
European Chemical
Societies Publishing

PV-EC. Even though the maximum power point controller is widely used in a conventional PV-powered hydrogen production system, this converter has several disadvantages such as complexity, energy transfer loss due to the line impedance, and high cost.[9b,30] Therefore, developing a direct-coupled PV-EC system showing the highest operating power is important. This review article does not deal with a converter-assisted PV-powered hydrogen production system.

2.4. Different types of PV-powered water splitting

Photovoltaic-driven hydrogen production is possible with many different device configurations. This review article covers only configurations in which the PV part can provide sufficient voltage for spontaneous water splitting. Here, the required voltage in the PV part is provided either by a lateral series connection of several single-junction solar cells,[37] or by a vertically integrated multijunction structure.[38] However, what is not considered in this article are configurations in which PV cells are coupled with photoanodes or photocathodes,[39] and systems based on concentrating PV (pros and cons of different these types of PV-based water splitting devices are shown in Table S1).[31] Roughly, PV-powered water splitting devices can be classified into four different types, as schematically described in Figure 4.

The 'type a' device (Figure 4a) consists of the series connection of PV module and electrolyzer (shown here membrane-based electrolyzer). An electron/hole pair generated by PV is directly transferred to the electrolyzer via externally connected wires. The transferred electron/hole pair is used in the cathode/anode of the electrolyzer system to split water into hydrogen and oxygen. Such PV-electrolyzer combinations are most common in the field of PV-powered water splitting, as they are relatively easy to set up compared to other technologies. Also, this type does not suffer from chemically induced degradation of the PV (against electrolyte), which is problematic when there is direct contact between PV and EC (in the electrolyte) as in fully integrated concepts.

In the case of wafer-based silicon solar cells, most demonstrators consist of three[32] or four[33] single junction solar cells connected in series, as they can provide a voltage of about $600 \sim 650$ mV at a current close to their optimal operating point. These devices provide enough voltage in total to drive commercial electrolyzers, which require a voltage of $1.8 \sim 2.0$ V for operation.[34] A recently developed device consisting of three silicon solar cells (in this case, silicon heterojunction solar cells) and a lab-scale alkaline electrolyzer has achieved a STH efficiency of around 13–15%.[32] For comparison, devices with four c-Si cells connected in series typically only achieve STH efficiencies around $9 \sim 10\%$ due to increased coupling losses.[33a,35]

Similarly, PV-EC devices with different numbers of CIGS cells connected in series have been studied in the literature. Again, devices with a smaller number of cells achieve higher STH efficiency ($> 10\%$)[36] compared to 4.4%,[6d] as long as sufficient voltage is generated for spontaneous water splitting. In

addition to commercially available PV technologies, studies can also be found using not yet commercially available technology, such as halide perovskite solar cells[37] Unlike other solar cell types, a single junction perovskite cell can generate an exceptionally high photovoltage in the range of up to 1.5 V. This means that two cells are sufficient for spontaneous water splitting. Devices based on perovskite solar cells with STH efficiency of 12.3% can be found in the literature.[37a]

Device "type b" (Figure 4b) consists of multi-junction PV cells as photoanode (or photocathode) providing a sufficiently high voltage for spontaneous water splitting. In addition, a cathode (or anode) is used, facing the photoanode (or photocathode). Both are electrically connected with a cable. This type was developed from a PEC approach consisting of a semiconductor that requires an external bias to operate.

Both types (type a, b) shown so far require at least one external wire connection to operate the system. To further simplify the structure of the device to reduce cost, much research has been done by placing all materials on one substrate (Figure 4c and d). This type of structure is commonly referred to as a "wireless (or non-wired)" device.[38]

In device type c (Figure 4c), the photoactive region (here the photocathode is shown on the right side in the upper figure) is physically separated from the anode but electrically connected via a transparent conductive electrode (TCO; SnO_2). The side-by-side geometry of the catalysts results in a position-dependent length of the ion diffusion path between the cathode and anode. This side-by-side configuration inevitably includes a photovoltaically inactive region (here NiFeO for water oxidation on the left), which reduces the aperture area related to STH efficiency, in whose calculation the inactive regions must be included.

In the "type d" device (Figure 4d), the PV part is embedded between the two catalysts (without external wire), which means that the light must be guided to the photoactive part through one of the catalysts, and the gas bubbles formed at the catalyst. As this configuration is generally assigned as the PEC approach, which is the future definition of integrated PV-EC. This configuration leads to optical losses that could be partially mitigated by concepts such as ultra-thin catalyst[39] or delocalized catalyst.[40] Furthermore, this concept has the longest ion diffusion path since the ions have to diffuse around the device from one side to the other.

2.5. Consideration for scalable PV-EC devices

In contrast to the fabrication of lab-scale PV-EC devices (~ a few cm²), several things need to be considered for square meter-scale systems. This section discusses the factors to consider for a scalable PV-EC device. A prerequisite for the future success of PV-EC systems is that the cost of H_2 production using such systems must be comparable to commercially available production processes (i.e., steam reforming; ~$1 per kg).[44] Estimates show that PV-EC systems can achieve ~$0.90 per kg using noble metal catalysts (Pt/IrO₂) if the total system is well optimized. With catalysts made of earth-abundant materials (Ni/

Co$_3$O$_4$), even costs as low as \$0.54 per kg are possible.[21a] The calculations also show that in optimized systems, the hydrogen production cost is dominated by the price of the PV components. Since the prices of PV modules are steadily decreasing, a further reduction of the hydrogen production costs for PV-EC systems can also be assumed.[45] Carbon taxes[46] have already been introduced or are planned to be introduced worldwide, so PV-driven H$_2$ production could be very economical in the near future.[12,21a,23a] Another aspect that needs to be considered in scaling up is appropriate fabrication processes. While laboratory-scale PV-EC systems can also use processes that lead to inhomogeneous layers or device properties, a homogeneous fabrication process is of great importance for large-scale systems. Established technologies such as chemical vapor deposition (CVD), cathode dicing (PVD), and sputtering can be used for both the PV and EC parts of the system. In contrast with the PV system where the quality of the thin film is important to reduce the resistance, much cheaper methods such as the electrochemical approach (i.e., electrodeposition) or hydrothermal method can be considered for practical device design for EC.[47] Another issue closely related to the fabrication process is the chemical stability of the protective coatings. These coatings provide the chemical separation between the PV part and the EC part (electrolyte) depending on the system concept used. If this barrier is not stable over the long term, even the smallest pinholes in the protective layer can represent a penetration path for the electrolyte used in the EC part. Once penetrated from the EC part to the PV part, the electrolyte can lead to chemical decomposition of the PV part and ultimately to failure of the entire system.[48]

Last but not least, safe fuel separation and collection should be considered when scaling up spatially distributed PV-EC systems.[7a] Fuel separation is achieved by implementing a proton or anion exchange membrane, which typically leads to increased overpotentials.

Figure 5 summarizes the four briefly stated consideration factors. It should be noted that all consideration factors for PV and EC are dependent on the selected system architectures.

In the following sections, three demonstrated system architectures would be presented. A few representative exam-

Figure 5. Consideration factors for the upscaling of PV-EC-devices.

ples are presented in each section. The most impressive demonstrations of PV-driven EC devices are summarized in Figure 9. Reported STH efficiencies (depending on the type of PV absorber) are shown as a function of light absorber geometric size. A complete list of studies conducted at a large-scale (PV > 50 cm^2) is given in Table 1. Notably, all the demonstrated systems in Table 1 are based on the direct coupling of PV and EC and are listed in chronological order. The demonstrations with auxiliary devices (such as converter or battery) are not considered in the table. Additionally, one possible but not yet realized architecture will be discussed in Section 2.9.

2.6. Upscaled (PV area > 50 cm^2) PV-EC device: system architecture (I)

Figure 6a shows a schematic drawing of how the most common PV-EC device 'type a' can be fabricated on a large-scale. In recent decades, a lot of upscaled demonstrations have been presented using this device type.[49] However, many used auxiliary devices. These types of systems with auxiliary devices are not considered in this section/review article.

Large-scale PV modules typically consist of single junction solar cells electrically connected in series and partially also in parallel. The number of cells connected defines the current and voltage produced by the module. To match the voltages and currents of the PV module with the electrolyzer in an upscaled PV-EC system of system architecture (I), the electrolyzer can be prepared in a series-parallel configuration. Some theoretical guidance has been proposed to optimize the design in a large-scale system, such as a linear approximation method,[50] the particle swarm optimization algorithm,[51] and a multi-objective nonlinear optimization approach.[52]

Several directly coupled large-scale PV-EC systems have been investigated (since 2007),[9] which mainly focused on how to position the intersection (operation) point of the PV part and EC part close to the maximum power point of the PV part. Unfortunately, most publications lack important information (e.g., size, PV efficiency, and STH efficiency).

Figure 6b shows the schematic of a directly coupled PV-EC device with a PV area of 0.74 m^2.[53] Here a CIGS solar panel is used, which consists of three parallel-connected submodules. This configuration allows for high currents at relatively low voltages of ∼20 V (at V_{mpp}), beneficial for the connected EC part. Several EC cells are also connected in series to match the intersection point to the PV$_{mpp}$. In contrast to conventional electrolyzers, which supply water at the anode and cathode, an alternative setup is used, which feeds water only at the cathode side. This could reduce the total hydrogen production cost by removing auxiliary equipment such as pumps, tubes, and gas separators.

Figures 6d and 6e schematically show the single electrolytic cell setup and a photo of a stack setup, respectively (here, 12 stacks are used to match the PV voltage). At an initial measurement, the maximum power point of the PV curve (red dotted line measured at 25 °C under 1013 W m^{-2} solar radiation) is well-

Table 1. List of directly PV and EC coupled demonstration systems (PV area > 50 cm^2). More demonstrations including converter can be found in ref. [53].

Year	PV Peak power [kWp]	Efficiency [%]	Type	Size	EC Type	Power [kW]	STH efficiency [%] /Stability	Area ratio (A_{EC}/A_{PV})	STH/PV efficiency ratio	Ref.
2007	2.7		c-Si PV module		PEM[a]	5.6				[9a]
2009	2.4			20.4 m^2	PEM	2.6				[9b]
2012	2.7				PEM					[58]
2013			4-lateral series connected c-Si PV module		PEM Pt—Pt (4 cm2) /water		6.18 (with J_{op}) / ~18 m (~5% loss)			[33b]
2014	0.12				PEM	0.26				[53]
2016		11.49 (1 cm^2)	2 lateral series connected TF-Si[b] (a-Si:H/μc-Si:H)[c] module	64 cm^2	EC cell NF/NF /1 m KOH		~3.9 (with gas) at 1 sun, R.T.[d] /3 h	0.75	0.34	[57a]
2017		10.2 (1 cm^2)	TF—Si (a-Si:H/a-Si:H/μc-Si:H) module	64 cm^2	EC cell IrO$_x$/Pt /1 m KOH		~4.8 (with J_{op}) at 1 sun, R.T. /80 m	0.79	0.47	[48]
2018		7.7 (64 cm^2)	TF—Si (a-Si:H/a-Si:H/μc-Si:H) module	64 cm^2	EC cell NiFeO$_x$/NiMo /1 m KOH		~5.1 (with I–V) at 1 sun, R.T. /10 m	0.79	0.66	[56]
2019			3 series connected c-Si module	58.5 cm^2	EC cell NiFeO$_x$/NiMo /1 m KOH		13.5	0.86		[59]
2019				1.6 m^2			15			[60]
2019		12.4	CIGS[e]	0.74 m^2	PEM (0.38 mg/cm^2 IrO$_2$; cathode: 0.13 mg/cm^2 Pt)		6.4~9.1		0.52~0.73	[53]
2020	0.27	17.5	c-Si	1.5 m^2	17 series connected PEM electrolyzers		9.4		0.54	[61]
2020		10.83 (2.25 cm^2)	7 neighbouring base unit consisting of 3-junction TF—Si (a-Si:H/a-Si:H/μc-Si:H) PV module	64 cm^2	EC cell NiFeMo/ NiFeMo /1 M KOH		~4.67 (with gas) at 1 sun, R.T./30 m	0.41	0.43	[57b]
2020	0.001–0.005	17.1	3 series connected c-Si module	294 cm^2	EC cell NiMo/NiFe /1 M KOH		3.4~10		0.2~0.58	[62]
2020			c-Si + CIGS	10 m^2			>10			[6k]
2020			c-Si	730 cm^2			13.5			[63]
2021		14.5	CIGS	100 cm^2	EC cell NiMoV/NiO /1 M KOH		11 /100 h	1	0.76	[65]

[a] PEM: Polymer electrolyte membrane electrolysis, [b] TF—Si: thin-film silicon, [c] (a-Si:H/μc-Si:H): hydrogenated amorphous and micro-crystalline Si, [d] R.T.: room temperature, [e] CIGS: Cu(In$_x$Ga$_{1-x}$)(S$_y$Se$_{1-y}$)$_2$.

matched with the polarization curve of the electrolyzer (green line). However, for elevated temperatures (91 °C), the voltage of PV significantly decreased, which led to a reduction in STH efficiency. To increase the total STH efficiency, Müller et al. also varied the number of electrolyzer cells. Finally, they found optimized conditions (a 10-cell stack for the temperature of 91 °C) with maximum STH efficiency of ~8.5%. Additionally,

they investigated thermally decoupled systems (PV at 20 °C and electrolyzer at 80 °C), which led to STH efficiency of ~9.1%.
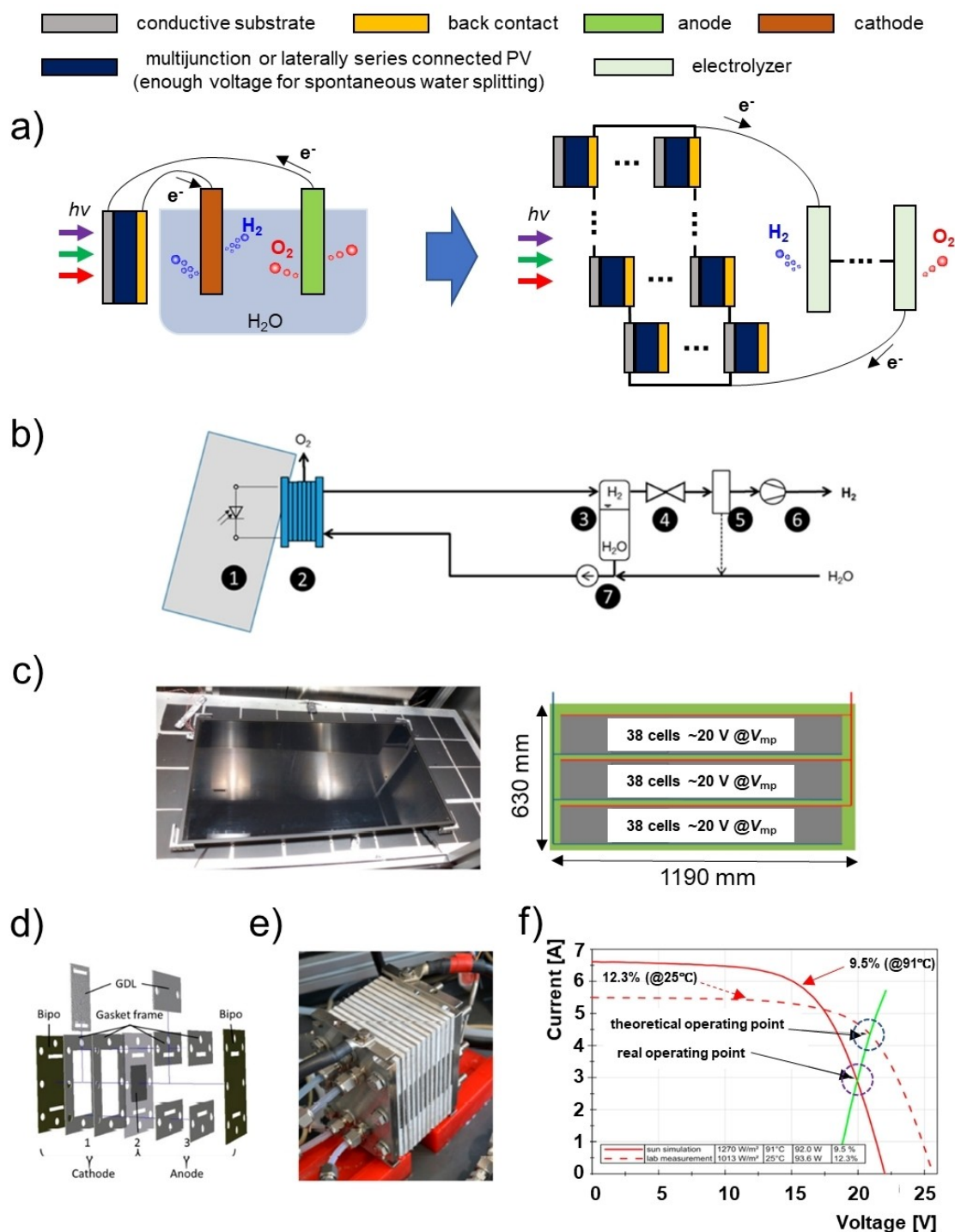
Figure 6. Upscaled (PV area > 50 cm²) system architecture (I). (a) Schematic drawing of the PV-EC device 'type a' (shown in Figure 4a) and related upscaling concept. (b) Schematic drawing of an advanced setup of PV-EC system with ① PV module; ② electrolysis cell/stack; ③ hydrogen separator; ④ valve for pressure control; ⑤ dehumidification; ⑥ compressor; ⑦ water circulation pump. (c) Photograph (left side) and configuration (right side) of CIGS PV panel used in upscaled PV-EC-system. A large CIGS solar panel (0.74 m²) is prepared with an effective voltage of ~20 V (at V_{mpp}). It consists of three parallel-connected CIGS submodules made of series-connected 38 cells. (d) A partial assembly sketch of the cell. (e) Photograph of a stack after assembling (f) Current-Voltage (I–V) curves of PV (red dotted line; initial curve at 25 °C, red line; at elevated temperatures due to illumination at 91 °C) and electrolyzer stack (green line). Reproduced from Ref. [53] Copyright (2019), with permission from Multidisciplinary Digital Publishing Institute.

ChemElectroChem

Review
doi.org/10.1002/celc.202200838

Chemistry Europe
European Chemical
Societies Publishing

2.7. Upscaled (PV area > 50 cm²) PV-EC device: system architecture (II)

As a second demonstrated case of upscaling, Figure 7a shows an approach to making a scalable PV-EC design from the device type 'b' (shown in Figure 4b). Here, a single multi-junction solar cell is scaled up to large areas for the PV part. However, such upscaling devices result in the problem that carriers must flow over large distances with the help of thin layers. This point is particularly problematic for the TCOs mostly used on the illuminated side of the PV part, where a good trade-off must be found between electrical (conductivity) and optical (transmittance) properties.[54] The long distances lead to high ohmic losses associated with resistance in the TCO, which results in a significant loss in fill factor FF of the PV part.[55]

Figure 7b shows a schematic cross-section of an upscaled device in which both issues (conductivity and transmittance) have been addressed. The device consists of an upscaled triple-junction a-Si:H/a-Si:H/μc-Si:H PV cell (64 cm² as aperture area) coupled to an EC part using inexpensive NiMo and NiFeO$_x$ as HER and OER catalysts. In order to reduce the Ohmic losses associated with the long conduction paths, a metal grid connected to the TCO was introduced, which consists of highly conductive silver. Notably, the metal grid was cut out of the used back contact by laser structuring. To protect the PV part against corrosion, a thin metal sheet (nickel) was introduced between the PV part and the EC part, which also acts as an electrical conductor. As schematically shown in Figure 7d, 64 individual square cells (each with an area of 1 cm²) were patterned and electrically connected in parallel on a 100 cm²
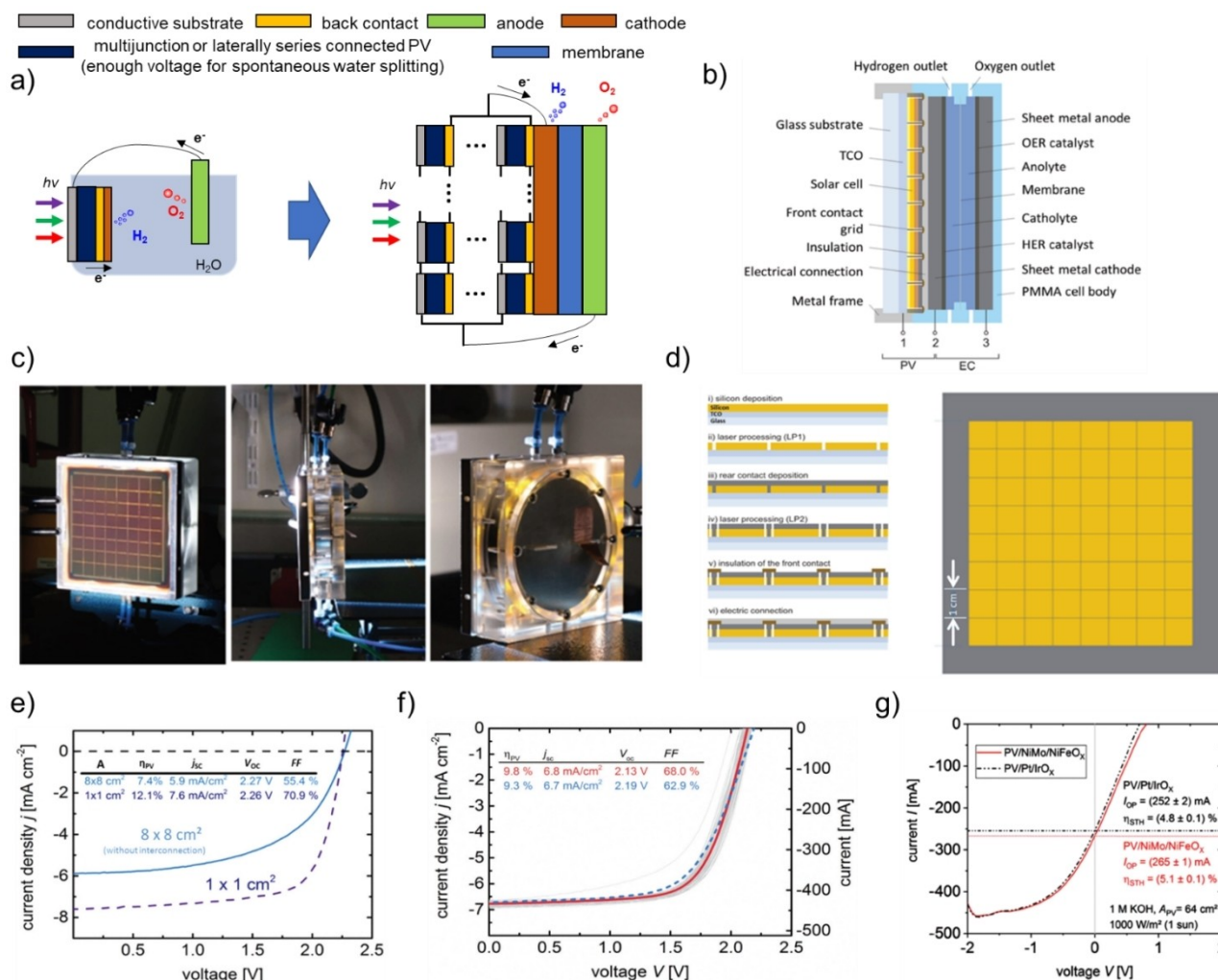

Figure 7. Upscaled (PV area > 50 cm²) system architecture (II). (a) Schematic drawing of the PV-EC device 'type b' (shown in Figure 4b) and related upscaling concept. (b) Schematic cross-section image of integrated PV-EC device using a thin-film a-Si:H/a-Si:H/μc-Si:H triple-junction PV (64 cm² aperture area, 100 cm² substrate area) as a power source. (c) Photographs of the fabricated upscaled PV-EC device from different angles; front view (left), side view (middle), and back view (right). (d) Schematic image of the fabrication process for the metal grid used in the upscaled thin-film a-Si:H/a-Si:H/μc-Si:H triple-junction PV (64 cm² aperture area) from a cross-sectional view (left) and corresponding front view with 64 parallel PV cells. (e) Current density-voltage (J-V) curves of a-Si:H/a-Si:H/μc-Si:H triple-junction PV with different sizes and without the metal grid. The results show a significant loss of short circuit current density and fill factor for larger size (8×8 cm²) than small (1×1 cm²). (f) J-V curves of different PV cells; 64 individual cells (1×1 cm² with grey lines), an average value of all cells (red line), and interconnected individual cells (dashed blue line). (g) I–V curves of PV-EC devices using earth-abundant NiMo/NiFeO$_x$ catalysts and Pt/IrO$_x$. Reproduced from Ref. [48, 56] Copyright (2017, 2018), with permission from Royal Society of Chemistry.

ChemElectroChem

Review
doi.org/10.1002/celc.202200838

**Chemistry
Europe**
European Chemical
Societies Publishing

(10 cm×10 cm) using laser scribing. For comparison, a large cell (8 cm×8 cm) without a metal grid was also fabricated. However, this device shows much lower solar to electricity (STE) conversion performance (Figure 7e) compared to the device with a metal grid (Figure 7f). The grid containing module integrated into the upscaled type 'b' device shows a STH efficiency of 5.1% with NiMo/NiFeO$_x$ (HER/OER) catalysts, which is even higher compared to a similar device using Pt/IrO$_x$ catalysts (Figure 7g).

2.8. Upscaled (PV area > 50 cm^2) PV-EC device: system architecture (III)

This section presents the scaling of a device corresponding to the device 'type c' (shown in Figure 4c). Figure 8a shows in a schematic representation how scaling can be achieved by simply repeating the base unit of the device 'type c'. In contrast to the device configuration shown in Figure 4c, a deliberate short circuit between the back and front contacts is introduced
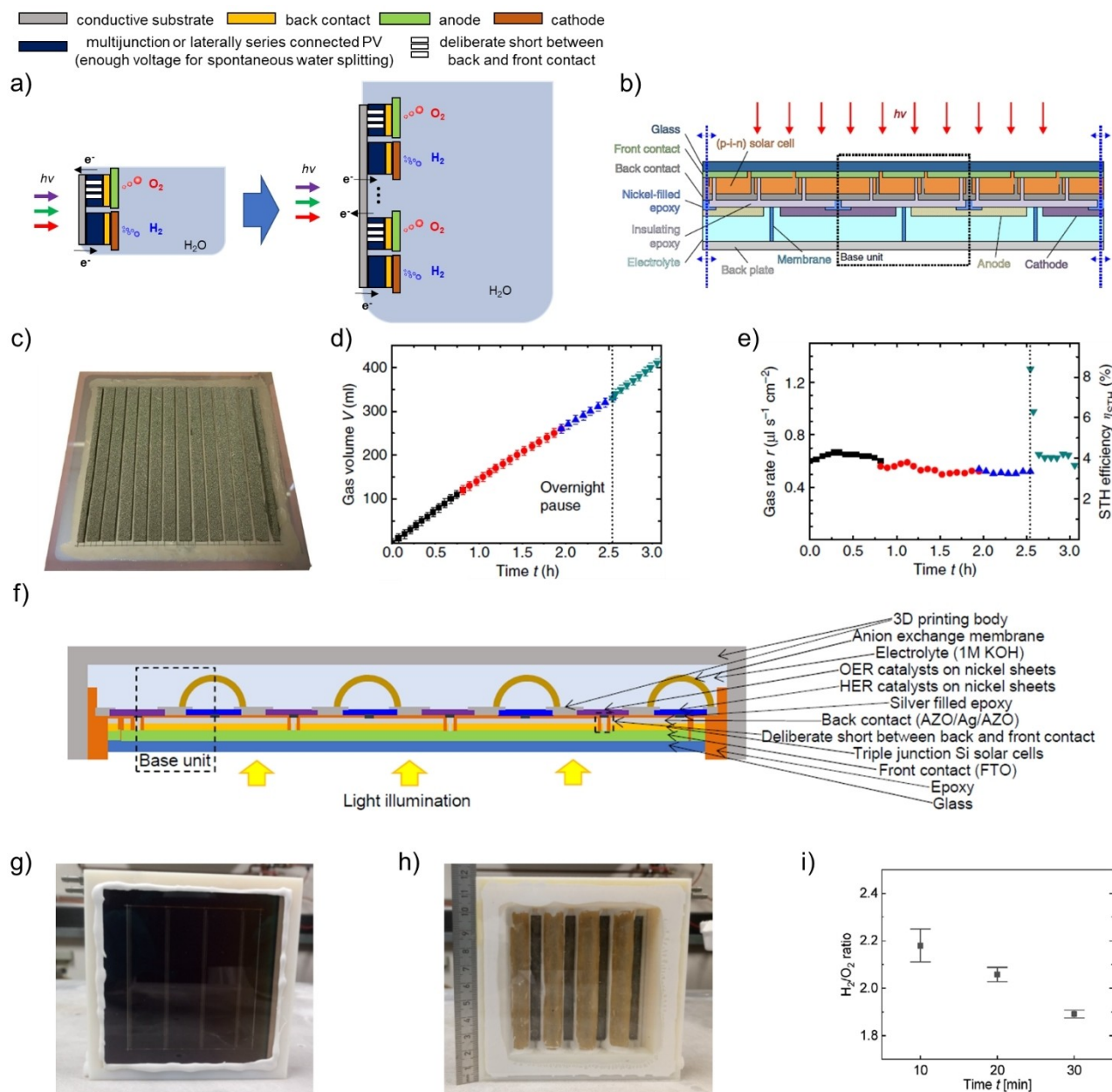

Figure 8. Upscaled (PV area > 50 cm^2) system architecture (III). (a) Schematic drawing of a base unit of a PV-EC device 'type c' (similarly shown in Figure 4c) and related upscaling concept. (b) A base unit consisting of three series-connected thin-film silicon solar cells, continuously mirrored and repeated for upscaling. Notably, the number of cell stripes in series can be adjusted depending on the PV materials and/or activity of EC for optimization of PV-EC coupling. (c) A photograph from the backside of the upscaled PV-EC device. In total, 13 based units were used. Each base unit consists of two series-connected a-Si:H/μc-Si:H tandem PV cells. (d) Collected gas volume, (e) the calculated gas rate and STH efficiency of the PV-EC device shown in Figure 8c as a function of time. (f) Schematic drawing of further development, including gas separation and better catalysts. (g) Front side view (PV) and (h) backside view (EC side) of the upscaling device. (i) Calculated STH efficiency of the PV-EC device (shown in Figures 8f-h) as a function of time. Reproduced from Ref. [57] Copyright (2016, 2020), with permission from Nature Publishing Group and Wiley.

ChemElectroChem

Review
doi.org/10.1002/celc.202200838

Chemistry Europe
European Chemical
Societies Publishing

locally by laser scribing to electrically connect the front contact of the PV part to the OER catalyst.

To the best of our knowledge, two scalable demonstrators using this design have been reported.[57] A proof of concept was first presented in ref.[57a] Results from this are shown in Figures 8b–e. Figure 8b shows the schematical design. Each base unit consists of laterally and/or vertically series-connected solar cells as an electrical power source and bare nickel foam as an electrocatalyst for water splitting. Adjacent base units share the catalysts. The photo of the upscaled device (nickel foam side) is shown in Figure 8c. Here the substrate has an area of 100 cm^2. The aperture area, including the dead area, is 64 cm^2 and the photoactive area is 52.8 cm^2. The upscaled device consisting of 13 side-by-side base units (one base unit consists of two a-Si:H/μc-Si:H tandem PV cells and nickel foam connected in series), has demonstrated an STH efficiency of ~3.9% for 3 h.

Although the upscaled demonstrator is significant progress compared to other laboratory cells, some crucial problems remained, such as the low STH efficiency and the inability to separate the gases. To overcome these two challenges, we recently developed a new device consisting of a triple-junction a-Si:H/a-Si:H/μc-Si:H-PV cell and a bifunctional NiFeMo water splitting catalyst (Figures 8f-i).[57b] Figure 8f shows a cross-sectional view of the newly developed device, similar to the device in Figures 8b and c. To achieve sufficient photovoltage for spontaneous water splitting without additional series connection of subcells, the two series-connected a-Si:H/μc-Si:H tandem PV cells were replaced by a triple-junction a-Si:H/a-Si:H/μc-Si:H PV cell. In addition, an earth-abundant NiFeMo catalyst was fabricated on the nickel foam to split water efficiently. An integrated PV-EC device with an aperture area of 64 cm^2 has shown an increased STH efficiency of ~4.7%, attributed to the better matching of the PV and EC I/V characteristics. The reason for the increase in STH efficiency is also due to the increase in photoactive area (from 52.8 to 56 cm^2) for a given aperture area (64 cm^2) caused by the reduction in the number of base units (from 13 to 7) and the elimination of the additional laser scribing process for the series connection of the subcells. However, due to the manual connection between the anode and the catalyst, an area with a width of 2 mm is still required for the connection, although the short produced by laser scribing only requires a few 100 μm of space. By making the connection between the anode and the catalyst more precisely, there is thus the possibility of further improving the STH efficiency. Unfortunately, this new device failed after 30 min due to the instability of the sealing materials and an inappropriate gas separation design rather than the degradation of PV and EC itself.

2.9. Scalable PV-EC device demonstration: the PECSYS project

In the last Sections (Figures 6–8), we explored how three different PV-EC approaches (Figures 4a–c) could be upscaled and showed realized examples with a PV area >50 cm^2 for each approach. In this section, we introduce one of the recent promising projects on direct PV-driven water splitting for H$_2$ production at a large-scale. The 'PECSYS' (Technology demonstration of large-scale photo-electrochemical system for solar hydrogen production) was a 4-year project (funded by the European Commission under the Horizon 2020 programme) that started in January 2017 and ended in December 2020. The final goal of the project PECSYS was to demonstrate an integrated PV-EC system at a large-scale (>10 m^2) for H$_2$ production with a Levelized cost of hydrogen (LCOH) production below 5 €/kg (16 g H$_2$/h STH efficiency >6% with <10% decrease after 6 months). More detailed information can be found at Ref.[6k] and.[64] Figure 9 shows reported STH efficiencies of different types of solar cells as function of light absorber geometric size.

An integrated PV-EC system using bifacial silicon heterojunction (SHJ) PV module and PEM electrolyzer is represented in Figure 10a.[32b] A picture of the integrated system is shown in Figure 10a ① where a 730 cm^2 minimodule (three amorphous Si/crystalline Si heterojunction cells) was directly connected with a PEM electrolyzer. The performance of two different PVs (monofacial and bifacial) was compared using current-voltage curves showing a much higher current in bifacial PV that leads to a higher STH efficiency than that of monofacial PV (Figure 10a ②). Time-dependent profiles (measured from 9 a.m. to 4 p.m.) of H$_2$ flux and STH efficiencies are presented in Figures 10a ③ and ④, respectively. The Figures clearly show that the integrated system with bifacial PV has a better performance with average STH efficiency (11 a.m. to 2 p.m.) of ~14% than that (~12%) of the monofacial PV integrated system.

An approach of silver-doped Cu(In,Ga)Se$_2$ (ACIGS) PV-driven alkaline water electrolysis is represented in Figure 10b.[65] A schematic drawing and a picture of the integrated PV-EC system are shown in Figures 10b ① and ②, respectively. In this study, Current-voltage curves of the 3-series connected cell (82 cm^2 active area) and 4-series connected cell (78 cm^2 active area) are presented in Figure 10a ③, the results show that the 3-cell integrated system has higher STH efficiency than the 4-cell
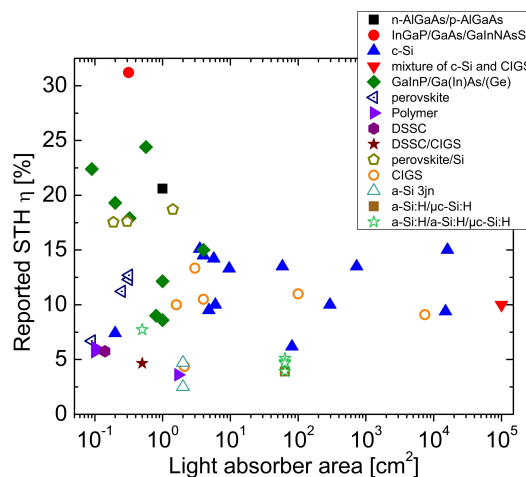

Figure 9. Reported STH efficiencies as function of light absorber geometric size.
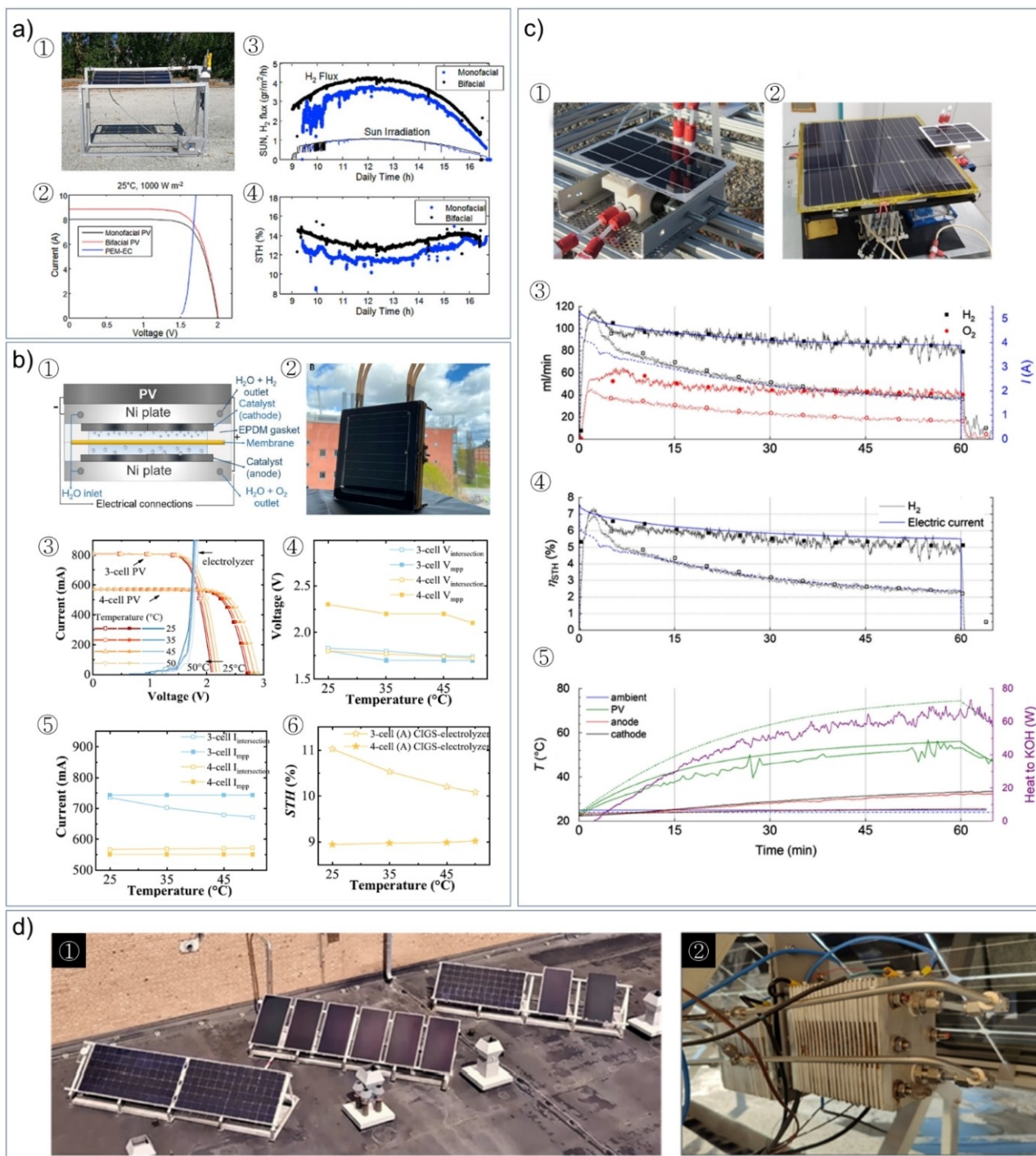
Figure 10. The demonstrated results of PV-driven water splitting for hydrogen production at a large-scale in the PECSYS project [technology demonstration of large-scale photo-electrochemical system for solar hydrogen production: https://www.helmholtz-berlin.de/projects/pecsys/]. (a) A demonstration of the integrated PV-EC system where a bifacial silicon heterojunction (SHJ) solar module is directly connected with a PEM electrolyzer. ① A picture ② Current-voltage characteristics of the integrated system. ③ SUN (Solar irradiation conditions) and H_2 flux during outdoor operation ④ The STH efficiencies of the coupled system. Reproduced from Ref. [32b] Copyright (2020), with permission from Elsevier. (b) A demonstration of the integrated PV-EC system where a (Ag,Cu)(In,Ga)Se2 ((A)CIGS) solar module is directly connected with a NiMoV (cathode) and NiO (anode)-based alkaline electrolyzer. ① A Schematic drawing ② A picture of the integrated PV-EC device. ③ Current versus voltage curves of the integrated system. ④ Voltage and ⑤ Current at maximum-power-point and intersection. ⑥ STH efficiencies of the integrated devices at different temperatures. Reproduced from Ref. [65] Copyright (2021), with permission from Elsevier. (c) A demonstration of the integrated PV-EC system where a silicon heterojunction (SHJ) solar module is directly connected with a NiMo (cathode) and $NiFeO_x$ (anode)-based alkaline electrolyzer. ① A photograph of an outdoor test setup (294 cm²) ② A picture of a scaled-up prototype (2600 cm²) ③ Products (oxygen and hydrogen) collection flow rate and operating current of the scaled-up prototype (2600 cm²) under 1 sun illumination ④ The STH efficiency of the prototype calculated from the volume of generated hydrogen and measured electric current. ⑤ Temperature measured at different positions of the integrated device as a function of time. Reproduced from Ref. [62] Copyright (2020), with permission from Royal Society of Chemistry. (d) A demonstration of the integrated PV-EC system where SHJ and CIGS solar modules are directly connected with a PEM electrolyzer. ① Aerial view of the final demonstrator in the PECSYS project ② A close-up photograph of the PEM electrolyzer connected to the back of the PV modules. Reproduced from Ref. [6k] Copyright (2022), with permission from Wiley.

ChemElectroChem

Review

doi.org/10.1002/celc.202200838

Chemistry Europe
European Chemical
Societies Publishing

system. Although the STH efficiency of the 4-cell integrated system is relatively lower than the 3-cells system, the 4-cell integrated system can be a good option if we consider operating with a higher yearly hydrogen yield due to a large margin for changes in light intensity and temperature. As shown in Figures 10b ④–⑥, voltage, current (at the intersection and maximum power point) and corresponding STH efficiency were monitored at different temperature conditions (25, 35, 45 °C), respectively. In the case of the 3-cell system, the intersection voltages showed similar values of the voltage at maximum power point compared to the 4-cell system (Figure 10b ④). In contrast to the 4-cell system, the intersection current dramatically decreased with increasing temperature (25 to 45 °C) because the intersection was placed much near at maximum power point compared to the 4-cell system (Figure 10b ⑤). Thereby, the corresponding STH efficiency of the 3-cell system varied with increased temperature (11 to ~10 %), whereas the STH efficiency was found to be more stable for a 4-cell system at different temperature conditions (Figure 10b ⑥).

An upscaled PV-EC device where silicon (a-Si/c-Si) heterojunction PV modules were directly connected with an alkaline electrolyzer is represented in Figure 10c.[62] A photo of the first prototype is shown in Figure 10c ① where PV has an area of 294 cm^2 and EC has a geometric electrode area of 50 cm^2. After the outdoor performance test, the group developed a larger PV-EC device with an area of 2600 cm^2 (Figure 10c ②) where better heat transfer was introduced via circulating the electrolyte. The effect of thermal integration (under simulated 1 sun illumination) in the larger prototype is shown in Figures 10c ③–④, the time transients of hydrogen and oxygen flow rates, operating current, and corresponding STH efficiency are represented, where continuous and/or solid symbols and dotted and/or unfilled symbols indicate with and without thermal integration, respectively. The hydrogen flow rate (in Figure 10c ③) was found to be 85 and 40 mL min^{-1} with and without thermal integration implying the stability of the device can be improved by introducing thermal integration. The time transients of the temperatures at different positions in the integrated PV-EC device are shown in Figure 10c ⑤. A substantial amount of heat transfer caused the decrease in PV temperature, whereas the temperature at electrolyte gradually increased over time.

Figure 10d shows a final demonstrator with over an area of 10 m^2 that was installed at Forschungzentrum Juelich (FZJ) where >10 m^2 PV array consisted of CIGS PV modules (Solibro Research AB) and a-Si/c-Si heterojunction PV modules (Enel Green Power) was directly coupled to PEM electrolyzer (FZJ).[6k] The final demonstrator was continuously operated and the amount of produced H$_2$ was monitored. The final integrated system exceeded the project target where average STH efficiency of around 10 % over 9 months was achieved (22 kg/H$_2$ in total period), and the device was found to be highly stable showing a performance degradation of less than 10 %.

2.10. Cost predictions

The cost of H$_2$ production would be one of the crucial factors to replace dominant energy carriers (i.e., fossil fuels) with H$_2$ produced by solar energy. PC and PEC concepts are undoubtedly considered cost-competitive if the device meets the requirements of efficiency and lifetime.[7a,66] However, these concepts are still evolving research fields, thereby reliable predictions at a large-scale can be more difficult. In this section, economic analysis is briefly introduced based on two PV-electrolysis articles[21a,67] shown in Figure 11.

It is generally accepted that the total H$_2$ production cost needs to be provided for each of the pathways based on the environmental life cycle assessment method.[67]

The LCOH analysis of H$_2$ production via PV-driven water electrolysis is conducted using the below equation[69] and the results are represented in Figure 11e considering six different scenarios (Figure 11a-d and including two different sub-configurations: off grid PV + alkaline and PEM limited operation).[67] The LCOH (in €/kg H$_2$) is calculated using Equation 13.

$$\text{LCOH (in €/kg H}_2) : \frac{I + \sum_{t=1}^{n} \frac{A_t}{(1+i)^t}}{\sum_{t=1}^{n} H_t} \tag{13}$$

Where I is the initial investment for the system in €, A_t is annual costs (operation and replacement) in year t in €, H_t is hydrogen produced in year t in kg, i is discount rate in % (assumed to be 4 % for Germany based on the reference,[69] n is system lifetime in years (20 years for all the scenarios), and t is time in year.

An integrated techno-economic analysis (Figure 11e) indicates that the H$_2$ production costs of grid connected systems [30.41~57.61 €/kg H$_2$] are much more expensive than off grid systems [6.23~7.86 €/kg H$_2$] because the additional battery backup option (battery contribution is above 50 % in total price in Figure 11f) is considered in off grid systems for enabling continuous power supply.[67] Even though off grid systems have a considerable impact on greenhouse gas (GHG) emissions (CO$_2$ emission per kg H$_2$ production)[68] and have a positive effect on the STH efficiency as well,[6l,70] the total cost seems much higher than that of grid-based systems. Therefore, further optimization studies on off grid based integrated systems need to be conducted especially in reducing the battery price. Also, the direct PV-EC coupling system mainly introduced in the current review article can be considered as an alternative to the option of battery integrated system.

As shown in Figure 11h, the H$_2$ cost of the different PV-EC systems was compared, which was conducted through the H$_2$ cost analysis approach shown in the bottom image and description in Figure 11g.[21a] Where the PV performance according to the illumination conditions of Arizona in the United States was considered, a membrane-electrode assembly (MEA) configuration with loaded catalysts is assumed to calculate STH efficiency. The area ratio of EC and PV components (here F indicates a ratio of EC and PV) is an important indicator as these parameters determine how efficiently the PV-EC devices can be operated. Naturally, if the
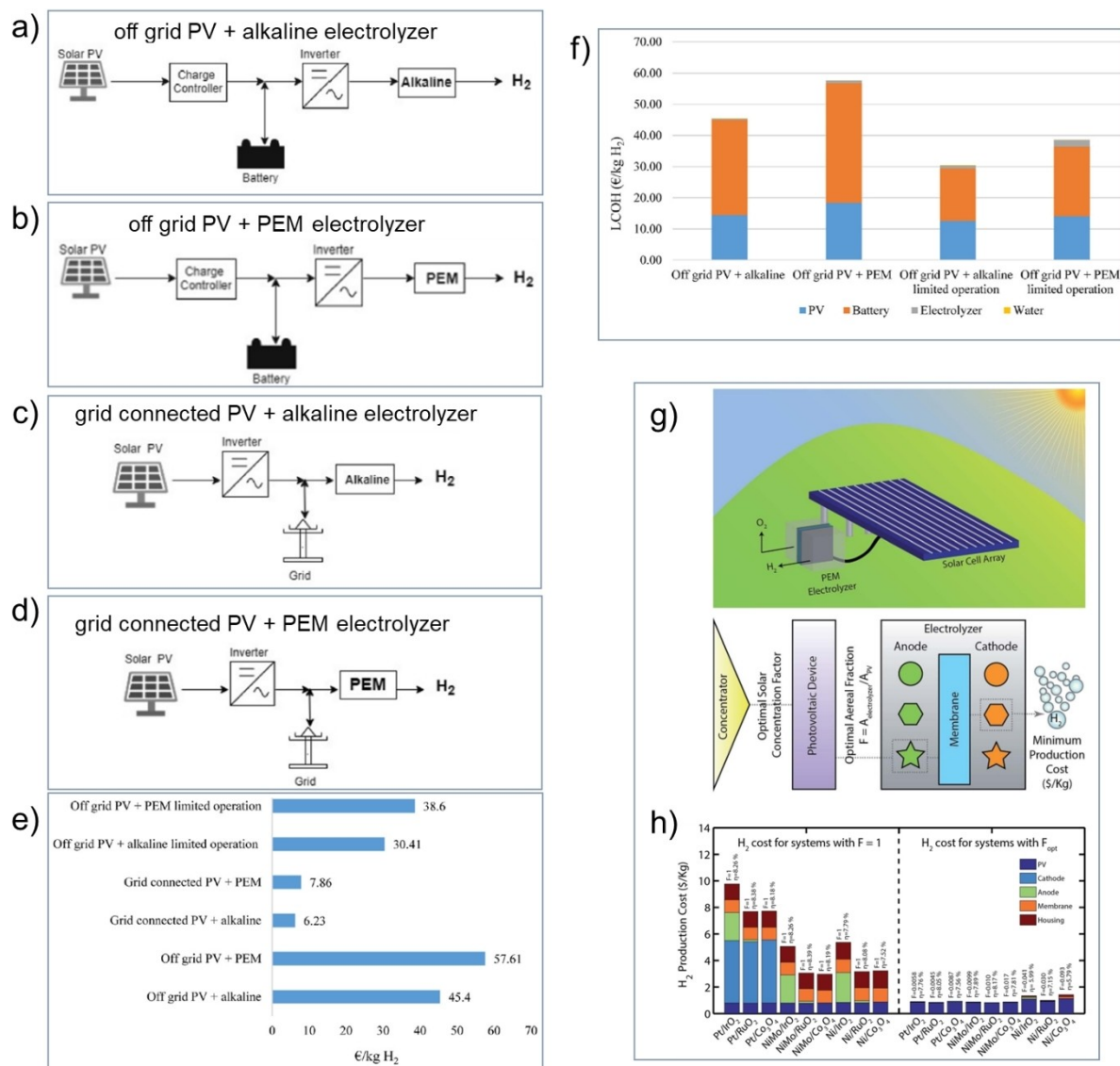
ChemElectroChem

Review
doi.org/10.1002/celc.202200838

Chemistry Europe
European Chemical
Societies Publishing

Figure 11. Schemes of (a) off grid PV+alkaline electrolyzer, (b) off grid PV+PEM electrolyzer, (c) grid connected PV+alkaline electrolyzer, (d) grid connected PV+PEM electrolyzer, and (e) Levelized cost of hydrogen (LCOH) calculated at different scenarios including limited operation modes (a–d). Reproduced from Ref. [67] Copyright (2021), with permission from Elsevier. (f) A H_2 production cost analysis approach of PV-EC system and (g) a cost analysis of the PV-EC systems having different catalytic components at F (ratio between electrolysis area and PV area) = 1 and F_{opt} (optimized F). These results show the cost of PV would be dominant when F is well optimized. Reproduced from Ref. [21a] Copyright (2014), with permission from Royal Society of Chemistry. (f) LCOH cost distribution for off grid systems. (g) A H2 production cost analysis approach of PV-EC system and (h) a cost analysis of the PV-EC systems having different catalytic components at F (ratio between electrolysis area and PV area) = 1 and Fopt (optimized F).

area of EC increases for a given size of PV, the STH efficiency increases as the electrochemical load are lowered in the integrated device. The detailed calculation process can be found in the analysis article.[21a] In the case of F = 1 (left image in Figure 11h), the H_2 cost for the integrated system can be varied based on the different catalytic components (Figure 11h) and can be dominated by the cost of catalysts. Interestingly, the cost of H_2 production can be reduced to as low as $0.54 per kg if the total PV-EC system is well optimized (Ni/Co_3O_4 as the catalysts in the right image in Figure 11h), which can make the current H_2 market share goes up. Additionally, the PV-EC approach would be more promising if we consider the growing global demand for renewable energy, which needs to reduce

the amount of CO_2 production, and a CO_2 tax should be considered in the future when comparing the total cost of energy carriers, which make the PV-EC approach more competitive.

3. Summary and Outlook

This review article delivers knowledge about the production of hydrogen-powered by a clean energy source of solar energy. We explore the three different types (i.e., PC, PEC, and PV-EC) of solar-driven water splitting and particularly focus on the aspect of the upscaled (with photovoltaic area > 50 cm²) PV-EC water

ChemElectroChem

Review
doi.org/10.1002/celc.202200838

Chemistry Europe
European Chemical
Societies Publishing

splitting devices. Substantial improvements have been made in the field of solar water splitting for several decades. Even though PC and PEC technologies are improving day by day, the STH efficiencies are still lower than the target value of at least 10% for enabling the solar water splitting system to penetrate markets. Additionally, demonstrations with PC and PEC approaches have been scaled up to around 1 m², which is not enough for commercialization. Several issues such as materials stability, the balance of systems, and device stability have arisen at such a large-scale. By contrast, the PV-EC approach for hydrogen production has already surpassed STH efficiency of 10% (19% with buried junction PV) and even reached over 30% with a combination of PV and PEM electrolyzers. Compared to the PC and PEC approaches that must be included in the electrolyte, the PV-EC approach has been much more stable since PV can be positioned outside the electrolyzer. Consequently, the PV-EC system can be a feasible approach in the short term (<10 years), and other solar-powered H₂ technologies can be deployed in the long term if they meet the requirements for scaling up the system.

Four different categories of unbiased PV-driven water splitting systems are introduced. Three different types of upscaling PV-electrolysis demonstrations and one possible system for upscaling architecture are presented in the main body. Even though different approaches and configurations are shown to be promising, each with its attractions, the open question remains; which type of PV-electrolysis will be dominant in the future? In our opinion, directly coupled PV-electrolysis system architecture (I) (shown in Figure 6) is expected to take control of future PV-powered hydrogen generation since this configuration has shown the most efficient and stable performance compared to other systems. As a part of particular purposes for generating hydrogen, wireless systems can also be used despite relatively low efficiency and stability as these systems have the advantage of being portable and easy to operate. The appropriate research and development of new materials and designs need to be continued to achieve a high level of efficiency and stability of the new devices.

Many countries have been investing in the hydrogen-based economy that is rapidly growing recently and/or already partially established as pilot projects. Establishing the hydrogen infrastructure is one of the most critical factors for a future full hydrogen economy. H₂ can be mainly transported via an industrial H₂ pipeline or a liquid container storing H₂ to a liquid organic hydrogen carrier (LOHC), and H₂-equipped filling stations will be filled by H₂ tanks, liquid H₂ tank trucks, or generated H₂ on site. If we use the distribution infrastructure of fuels that are already existed/or need to be modified a bit, we could reduce the total cost for H₂ production. Thereby it would not be a significant burden for expanding infrastructure. One of the key features of the hydrogen economy is that H₂ generation can be either centralized and distributed or can be balanced with a mixture of both. Although higher H₂ production efficiency can be obtained at centralized plants, there are downsides to using this approach, such as long-range transportation of H₂ and storage. These issues can be resolved by

converting H₂ to electricity that can be distributed. In the case of distributed H₂ generation such as PV-EC powered H₂ production at home or fuel station, while H₂ production efficiency is lower than that of a centralized approach, we don't need to consider long-range transportation, which could reduce the total cost for the use of H₂. The proper balance between central and distributed production depending on local circumstances can be of great significance in the future hydrogen economy.

Nomenclature

PV	photovoltaic
°C	degree Celsius
TW	terawatt
$MJ\,kg^{-1}$	megajoules per kilogram
PC	particulate
PEC	photoelectrochemical
PV-EC	PV-electrochemical
HER	hydrogen evolution reaction
OER	oxygen evolution reaction
aq	aqueous
l	liquid
g	gas
ΔG^0	change in Gibbs free energy
E_{CB}	conduction band energy
E_{VB}	valance band energy
E_{Fn}	quasi-Fermi level for electrons
E_{Fp}	quasi-Fermi level for holes
$h\nu$	solar energy
qV	photovoltage
qV_{pha}	photovoltage for photoanode
qV_{phc}	photovoltage for photocathode
E_g	bandgap
n-type	n-doped semiconductor
p-type	p-doped semiconductor
V_{PV}	voltage of PV
$H^+/H_2\ (-qE°)$	electrochemical thermodynamic potential of proton reduction
$O_2/H_2O\ (-qE°)$	electrochemical thermodynamic potential of water oxidation
$H^+/H_2\ (j)$	electrochemical potentials of proton reduction in coupled PV-EC device
H_2O/O_2	electrochemical potentials of water oxidation in coupled PV-EC device
$\eta_{HER}(j)$	overpotentials of HER
$\eta_{OER}(j)$	overpotentials of OER
SHE	standard hydrogen electrode
$kJ\,mol^{-1}$	kilojoule per mole
n_e	the number of electrons
F	Faraday constant
E^0	thermodynamic standard potential
M	mole
STH	solar to hydrogen
DC	direct current
J-V	current density-voltage

ChemElectroChem

Review

doi.org/10.1002/celc.202200838

Chemistry Europe
European Chemical
Societies Publishing

V_{oc}	open circuit voltage
J_{sc}	short-circuit current density
J_{op}	operating current density
μ_{th}	thermodynamic reaction potential
J_{PV}	output current density of PV
J_{EC}	input current density of EC
V_{EC}	input voltage of EC
J_0	dark saturation current density
n	diode ideality factor
V_{th}	thermal voltage
q	electron charge
T	temperature
k_b	Boltzmann constant
R_s	series resistance
R_{sh}	shunt resistance
R_{sol}	solution resistance
τ_{OER}	Tafel slope of OER
τ_{HER}	Tafel slope of HER
J_0^{OER}	exchange current density of OER
J_0^{HER}	exchange current density of HER
R	ideal constant
α	transfer coefficient
n_c	number of charge carriers
F	faradaic constant
η_{PV}	solar to electricity conversion efficiency
η_{EC}	efficiency of EC system
η_C	coupling efficiency between PV and EC
P_{sun}	solar irradiance
FF	fill factor
J_{mp}	current density at maximum power point
V_{mp}	voltage at maximum power point
V_{op}	voltage at operation point
J_{op}	current at operation point
P_{H2}	stored hydrogen power in PV-EC device
P_{KIN}	kinetic loss in PV-EC device
c-Si	crystalline silicon
CIGS	$Cu(In_xGa_{1-x})(S_ySe_{1-y})_2$
TCO	transparent conductive electrode
a-Si:H	hydrogenated amorphous silicon
μc-Si:H	hydrogenated micro-crystalline silicon
PEM	Polymer electrolyte membrane electrolysis
TF—Si	thin-film silicon
HER	Hydrogen Evolution Reaction
LDH	Double Layered Hydroxide
LSV	Linear Sweep Voltammetry
OER	Oxygen Evolution Reaction
PV	Photovoltaic
RHE	Reversible Hydrogen Electrode
SEM	Scanning Electron Microscope
STH	Solar-to-hydrogen
XPS	X-ray Photoelectron Spectroscopy

Acknowledgements

Conflict of Interest

The authors declare no conflict of interest.

[1] a) S. Chu, A. Majumdar, *Nature* **2012**, *488*, 294–303; b) C. McGlade, P. Ekins, *Nature* **2015**, *517*, 187–190.

[2] ADOPTION OF THE PARIS AGREEMENT can be found under https://unfccc.int/resource/docs/2015/cop21/eng/l09r01.pdf, **2015** (accessed 26 October 2022).

[3] a) S. Lewis Nathan, *Science* **2016**, *351*, aad1920; b) I. Roger, M. A. Shipman, M. D. Symes, *Nat. Chem. Rev.* **2017**, *1*, 0003.

[4] The potential of renewable alternatives to Greenhouse Gas (GHG) emitting fossil energy sources can be found under https://www.iea-shc.org/data/sites/1/publications/2015-11-A-Fundamental-Look-at-Supply-Side-Energy-Reserves-for-the-Planet.pdf, **2015** (accessed 26 October 2022).

[5] J. Yin, A. Molini, A. Porporato, *Nat. Commun.* **2020**, *11*, 4781.

[6] a) N. S. Lewis, D. G. Nocera, *Proc. Nat. Acad. Sci.* **2006**, *103*, 15729; b) M. G. Walter, E. L. Warren, J. R. McKone, S. W. Boettcher, Q. Mi, E. A. Santori, N. S. Lewis, *Chem. Rev.* **2010**, *110*, 6446–6473; c) T. R. Cook, D. K. Dogutan, S. Y. Reece, Y. Surendranath, T. S. Teets, D. G. Nocera, *Chem. Rev.* **2010**, *110*, 6474–6502; d) H. S. Jeon, J. H. Koh, S. J. Park, M. S. Jee, D.-H. Ko, Y. J. Hwang, B. K. Min, *J. Mater. Chem. A* **2015**, *3*, 5835–5842; e) Y. Wang, J. Liu, Y. Wang, Y. Wang, G. Zheng, *Nat. Commun.* **2018**, *9*, 5003; f) J. He, C. Janáky, *ACS Energy Lett.* **2020**, *5*, 1996–2014; g) Y. Dong, P. Duchesne, A. Mohan, K. K. Ghuman, P. Kant, L. Hurtado, U. Ulmer, J. Y. Y. Loh, A. A. Tountas, L. Wang, A. Jelle, M. Xia, R. Dittmeyer, G. A. Ozin, *Chem. Soc. Rev.* **2020**, *49*, 5648–5663; h) M. Ghoussoub, M. Xia, P. N. Duchesne, D. Segal, G. Ozin, *Energy Environ. Sci.* **2019**, *12*, 1122–1142; i) L. Wang, M. Xia, H. Wang, K. Huang, C. Qian, C. T. Maravelias, G. A. Ozin, *Joule* **2018**, *2*, 1055–1074; j) X.-W. Lv, L. Wang, G. Wang, R. Hao, J.-T. Ren, X. Liu, P. N. Duchesne, Y. Liu, W. Li, Z.-Y. Yuan, G. A. Ozin, *J. Mater. Chem. A* **2020**, *8*, 8868–8874; k) S. Calnan, R. Bagacki, F. Bao, I. Dorbandt, E. Kemppainen, C. Schary, R. Schlatmann, M. Leonardi, S. A. Lombardo, R. G. Milazzo, S. M. S. Privitera, F. Bizzarri, C. Connelli, D. Consoli, C. Gerardi, P. Zani, M. Carmo, S. Haas, M. Lee, M. Mueller, W. Zwaygardt, J. Oscarsson, L. Stolt, M. Edoff, T. Edvinsson, I. B. Pehlivan, *Solar RRL* **2022**, *6*, 2100479; l) O. Astakhov, S. N. Agbo, K. Welter, V. Smirnov, U. Rau, T. Merdzhanova, *J. Power Sources* **2021**, *509*, 230367; m) O. Astakhov, V. Smirnov, U. Rau, T. Merdzhanova, *Solar RRL* **2022**, *6*, 2100783.

[7] a) J. H. Kim, D. Hansora, P. Sharma, J.-W. Jang, J. S. Lee, *Chem. Soc. Rev.* **2019**, *48*, 1908–1971; b) C. Spöri, J. T. H. Kwan, A. Bonakdarpour, D. P. Wilkinson, P. Strasser, *Angew. Chem. Int. Ed.* **2017**, *56*, 5994–6021; *Angew. Chem.* **2017**, *129*, 6088–6117; c) I. Staffell, D. Scamman, A. Velazquez Abad, P. Balcombe, P. E. Dodds, P. Ekins, N. Shah, K. R. Ward, *Energy Environ. Sci.* **2019**, *12*, 463–491.

[8] A hydrogen perspective can be found under https://www.irena.org/-/media/Files/IRENA/Agency/Publication/2019/Sep/IRENA Hydrogen 2019.pdf, **2019** (accessed 26 October 2022).

[9] a) L. G. Arriaga, W. Martínez, U. Cano, H. Blud, *Int. J. Hydrogen Energy* **2007**, *32*, 2247–2252; b) R. E. Clarke, S. Giddey, F. T. Ciacchi, S. P. S. Badwal, B. Paul, J. Andrews, *Int. J. Hydrogen Energy* **2009**, *34*, 2531–2542.

[10] Q. Wang, K. Domen, *Chem. Rev.* **2020**, *120*, 919–985.

ChemElectroChem

Review

doi.org/10.1002/celc.202200838

Chemistry
Europe
European Chemical
Societies Publishing

[11] a) C. Jiang, S. J. A. Moniz, A. Wang, T. Zhang, J. Tang, *Chem. Soc. Rev.* **2017**, *46*, 4645–4660; b) D. Bae, B. Seger, P. C. K. Vesborg, O. Hansen, I. Chorkendorff, *Chem. Soc. Rev.* **2017**, *46*, 1933–1954.

[12] S. Ardo, D. Fernandez Rivas, M. A. Modestino, V. Schulze Greiving, F. F. Abdi, E. Alarcon Llado, V. Artero, A. Ayers, C. Battaglia, J.-P. Becker, D. Bederak, A. Berger, F. Buda, E. Chinello, B. Dam, V. Di Palma, T. Edvinsson, K. Fujii, H. Gardeniers, H. Geerlings, S. M. H. Hashemi, S. Haussener, F. Houle, J. Huskens, B. D. James, K. Konrad, A. Kudo, P. P. Kunturu, D. Lohse, B. Mei, E. L. Miller, G. F. Moore, J. Muller, K. L. Orchard, T. E. Rosser, F. H. Saadi, J.-W. Schüttauf, B. Seger, S. W. Sheehan, W. A. Smith, J. Spurgeon, M. H. Tang, K. van de Krol, P. C. K. Vesborg, P. Westerik, *Energy Environ. Sci.* **2018**, *11*, 2768–2783.

[13] a) H. Dau, C. Limberg, T. Reier, M. Risch, S. Roggan, P. Strasser, *ChemCatChem* **2010**, *2*, 724–761; b) N. Mahmood, Y. Yao, J.-W. Zhang, L. Pan, X. Zhang, J.-J. Zou, *Adv. Sci.* **2018**, *5*, 1700464.

[14] T. Shinagawa, A. T. Garcia-Esparza, K. Takanabe, *Sci. Rep.* **2015**, *5*, 13801.

[15] Y. Matsumoto, E. Sato, *Mater. Chem. Phys.* **1986**, *14*, 397–426.

[16] F. Song, L. Bai, A. Moysiadou, S. Lee, C. Hu, L. Liardet, X. Hu, *J. Am. Chem. Soc.* **2018**, *140*, 7748–7759.

[17] A. Kudo, Y. Miseki, *Chem. Soc. Rev.* **2009**, *38*, 253–278.

[18] a) Y. Yan, T. He, B. Zhao, K. Qi, H. Liu, B. Y. Xia, *J. Mater. Chem. A* **2018**, *6*, 15905–15926; b) C. G. Morales-Guio, L. Liardet, X. Hu, *J. Am. Chem. Soc.* **2016**, *138*, 8946–8957.

[19] a) Z. Wang, C. Li, K. Domen, *Chem. Soc. Rev.* **2019**, *48*, 2109–2125; b) T. Hisatomi, J. Kubota, K. Domen, *Chem. Soc. Rev.* **2014**, *43*, 7520–7535.

[20] a) Q. Wang, T. Hisatomi, Q. Jia, H. Tokudome, M. Zhong, C. Wang, Z. Pan, T. Takata, M. Nakabayashi, N. Shibata, Y. Li, I. D. Sharp, A. Kudo, T. Yamada, K. Domen, *Nat. Mater.* **2016**, *15*, 611–615; b) K. Maeda, *ACS Catal.* **2013**, *3*, 1486–1503.

[21] a) C. A. Rodriguez, M. A. Modestino, D. Psaltis, C. Moser, *Energy Environ. Sci.* **2014**, *7*, 3828–3835; b) A. Berger, R. A. Segalman, J. Newman, *Energy Environ. Sci.* **2014**, *7*, 1468–1476.

[22] S. M. Thalluri, L. Bai, C. Lv, Z. Huang, X. Hu, L. Liu, *Adv. Sci.* **2020**, *7*, 1902102.

[23] a) J. W. Ager, M. R. Shaner, K. A. Walczak, I. D. Sharp, S. Ardo, *Energy Environ. Sci.* **2015**, *8*, 2811–2824; b) F. Urbain, V. Smirnov, J.-P. Becker, A. Lambertz, F. Yang, J. Ziegler, B. Kaiser, W. Jaegermann, U. Rau, F. Finger, *Energy Environ. Sci.* **2016**, *9*, 145–154.

[24] F. M. Sapountzi, J. M. Gracia, C. J. Weststrate, H. O. A. Fredriksson, J. W. Niemantsverdriet, *Prog. Energy Combust. Sci.* **2017**, *58*, 1–35.

[25] a) Assessment of Hydrogen Production Costs from Electrolysis can be found under https://theicct.org/sites/default/files/publications/final_icct2020_assessment_of%20_hydrogen_production_costs%20v2.pdf; **2020** (accessed 26 October 2022); b) A cost perspective of hydrogen can be found under https://hydrogencouncil.com/wp-content/uploads/2020/01/Path-to-Hydrogen-Competitiveness_Full-Study-1.pdf; **2020** (accessed 26 October 2022); c) The U. S. Department of Energy (DOE) technical targets and example cost contributions for hydrogen production from water electrolysis can be found under https://www.energy.gov/eere/fuelcells/doe-technical-targets-hydrogen-production-electrolysis, (accessed 26 October 2022).

[26] Y. Surendranath, D. K. Bediako, G. Nocera Daniel, *Proc. Nat. Acad. Sci.* **2012**, *109*, 15617–15621.

[27] K. Sayama, Y. Miseki, *Synthesiology* **2014**, *7*, 79–91.

[28] T. Winkler Mark, R. Cox Casandra, G. Nocera Daniel, T. Buonassisi, *Proc. Nat. Acad. Sci.* **2013**, *110*, E1076–E1082.

[29] F. Urbain, Ph.D. Thesis, RWTH Aachen University, Aachen **2016**, https://publications.rwth-aachen.de/record/660412/files/660412.pdf.

[30] a) M. J. Khan, M. T. Iqbal, *Renewable Energy* **2005**, *30*, 835–854; b) O. Astakhov, T. Merdzhanova, L.-C. Kin, U. Rau, *Sol. Energy* **2020**, *206*, 732–740.

[31] a) A. Nakamura, Y. Ota, K. Koike, Y. Hidaka, K. Nishioka, M. Sugiyama, K. Fujii, *Appl. Phys. Express* **2015**, *8*, 107101; b) J. Jia, L. C. Seitz, J. D. Benck, Y. Huo, Y. Chen, J. W. D. Ng, T. Bilir, J. S. Harris, T. F. Jaramillo, *Nat. Commun.* **2016**, *7*, 13237.

[32] a) M. Lee, X. Ding, S. Banerjee, F. Krause, V. Smirnov, O. Astakhov, T. Merdzhanova, B. Klingebiel, T. Kirchartz, F. Finger, U. Rau, S. Haas, *Adv. Mater. Technol.* **2020**, *5*, 2000592; b) S. M. S. Privitera, M. Muller, W. Zwaygardt, M. Carmo, R. G. Milazzo, P. Zani, M. Leonardi, F. Maita, A. Canino, M. Foti, F. Bizzarri, C. Gerardi, S. A. Lombardo, *J. Power Sources* **2020**, *473*, 228619; c) J.-W. Schüttauf, M. A. Modestino, E. Chinello, D. Lambelet, A. Delfino, D. Dominé, A. Faes, M. Despeisse, J. Bailat, D. Psaltis, C. Moser, C. Ballif, *J. Electrochem. Soc.* **2016**, *163*, F1177-F1181; d) G. Heremans, C. Trompoukis, N. Daems, T. Bosserez, I. F. J. Vankelecom, J. A. Martens, J. Rongé, *Sustain. Energy Fuels* **2017**, *1*, 2061–2065;

e) S. Nordmann, A. Berghoff, A. Hessel, B. Zielinsk, J. John, S. Starschich, J. Knoch, *Sol. Energy Mater. Sol. Cells* **2019**, *191*, 422–426.

[33] a) R. Cox Casandra, Z. Lee Jungwoo, G. Nocera Daniel, T. Buonassisi, *Proc. Nat. Acad. Sci.* **2014**, *111*, 14057–14061; b) K. Fujii, S. Nakamura, M. Sugiyama, K. Watanabe, B. Bagheri, Y. Nakano, *Int. J. Hydrogen Energy* **2013**, *38*, 14424–14432.

[34] K. Zeng, D. Zhang, *Prog. Energy Combust. Sci.* **2010**, *36*, 307–326.

[35] H. Song, S. Oh, H. Yoon, K.-H. Kim, S. Ryu, J. Oh, *Nano Energy* **2017**, *42*, 1–7.

[36] T. J. Jacobsson, V. Fjällström, M. Sahlberg, M. Edoff, T. Edvinsson, *Energy Environ. Sci.* **2013**, *6*, 3676–3683.

[37] a) J. Luo, J.-H. Im, T. Mayer Matthew, M. Schreier, K. Nazeeruddin Mohammad, N.-G. Park, S. D. Tilley, J. Fan Hong, M. Grätzel, *Science* **2014**, *345*, 1593–1596; b) T. Sharifi, C. Larsen, J. Wang, W. L. Kwong, E. Gracia-Espino, G. Mercier, J. Messinger, T. Wågberg, L. Edman, *Adv. Energy Mater.* **2016**, *6*, 1600738.

[38] Y. Reece Steven, A. Hamel Jonathan, K. Sung, D. Jarvi Thomas, J. Esswein Arthur, J. H. Pijpers Joep, G. Nocera Daniel, *Science* **2011**, *334*, 645–648.

[39] C. G. Morales-Guio, M. T. Mayer, A. Yella, S. D. Tilley, M. Grätzel, X. Hu, *J. Am. Chem. Soc.* **2015**, *137*, 9927–9936.

[40] S. Oh, H. Song, J. Oh, *Nano Lett.* **2017**, *17*, 5416–5422.

[41] O. Khaselev, A. Turner John, *Science* **1998**, *280*, 425–427.

[42] Y. Yamada, N. Matsuki, T. Ohmori, H. Mametsuka, M. Kondo, A. Matsuda, E. Suzuki, *Int. J. Hydrogen Energy* **2003**, *28*, 1167–1169.

[43] G. H. Lin, M. Kapur, R. C. Kainthla, J. O. M. Bockris, *Appl. Phys. Lett.* **1989**, *55*, 386–387.

[44] M. Kayfeci, A. Keçebaş, M. Bayat, in *Solar Hydrogen Production* (Eds.: F. Calise, M. D. D'Accadia, M. Santarelli, A. Lanzini, D. Ferrero), Academic Press, 2019, 45–83.

[45] Recent Facts about Photovoltaics in Germany can be found under https://www.ise.fraunhofer.de/content/dam/ise/en/documents/publications/studies/recent-facts-about-photovoltaics-in-germany.pdf, **2021** (accessed 26 October 2022).

[46] N. Kaufman, A. R. Barron, W. Krawczyk, P. Marsters, H. McJeon, *Nat. Clim. Change* **2020**, *10*, 1010–1014.

[47] Y. Peng, K. Jiang, W. Hill, Z. Lu, H. Yao, H. Wang, *ACS Appl. Mater. Interfaces* **2019**, *11*, 3971–3977.

[48] J. P. Becker, B. Turan, V. Smirnov, K. Welter, F. Urbain, J. Wolff, S. Haas, F. Finger, *J. Mater. Chem. A* **2017**, *5*, 4818–4826.

[49] a) A. Brinner, H. Bussmann, W. Hug, W. Seeger, *Int. J. Hydrogen Energy* **1992**, *17*, 187–197; b) P. A. Lehman, C. E. Chamberlin, G. Pauletto, M. A. Rocheleau, *Int. J. Hydrogen Energy* **1997**, *22*, 465–470; c) A. Szyszka, *Int. J. Hydrogen Energy* **1998**, *23*, 849–860; d) J. P. Behrmann, A. Szyszka, *Int. J. Proj. Manag.* **1993**, *11*, 49–56; e) W. Stahl, K. Voss, A. Goetzberger, *Sol. Energy* **1994**, *52*, 111–125; f) C. Meurer, H. Barthels, W. A. Brocke, B. Emonts, H. G. Groehn, *Sol. Energy* **1999**, *67*, 131–138; g) P. Hollmuller, J.-M. Joubert, B. Lachal, K. Yvon, *Int. J. Hydrogen Energy* **2000**, *25*, 97–109; h) A. M. Chaparro, J. Soler, M. J. Escudero, E. M. L. de Ceballos, U. Wittstadt, L. Daza, *J. Power Sources* **2005**, *144*, 165–169.

[50] O. Atlam, F. Barbir, D. Bezmalinovic, *Int. J. Hydrogen Energy* **2011**, *36*, 7012–7018.

[51] F. Sayedin, A. Maroufmashat, R. Roshandel, S. S. Khavas, *Int. J. Sustain. Energy* **2016**, *35*, 566–582.

[52] A. Maroufmashat, F. Sayedin, S. S. Khavas, *Int. J. Hydrogen Energy* **2014**, *39*, 18743–18757.

[53] M. Müller, W. Zwaygardt, E. Rauls, M. Hehemann, S. Haas, L. Stolt, H. Janssen, M. Carmo, *Energies* **2019**, *12*, 4150.

[54] D. S. Ginley, C. Bright, *MRS Bull.* **2000**, *25*, 15–18.

[55] G. T. Koishiyev, J. R. Sites, *Sol. Energy Mater. Sol. Cells* **2009**, *93*, 350–354.

[56] K. Welter, N. Hamzelui, V. Smirnov, J. P. Becker, W. Jaegermann, F. Finger, *J. Mater. Chem. A* **2018**, *6*, 15968–15976.

[57] a) B. Turan, J.-P. Becker, F. Urbain, F. Finger, U. Rau, S. Haas, *Nat. Commun.* **2016**, *7*, 12681; b) M. Lee, B. Turan, J.-P. Becker, K. Welter, B. Klingebiel, E. Neumann, Y. J. Sohn, T. Merdzhanova, T. Kirchartz, F. Finger, U. Rau, S. Haas, *Adv. Sustainable Syst.* **2020**, *4*, 2000070.

[58] T. Maeda, H. Ito, Y. Hasegawa, Z. Zhou, M. Ishida, *Int. J. Hydrogen Energy* **2012**, *37*, 4819–4828.

[59] F. Finger, K. Welter, F. Urbain, V. Smirnov, B. Kaiser, W. Jaegermann, *Z. Phys. Chem.* **2020**, *234*, 1055–1095.

[60] A large hydrogen panel from KU Leuven can be found under https://nieuws.kuleuven.be/en/content/2019/belgian-scientists-crack-the-code-for-affordable-eco-friendly-hydrogen-gas, **2019** (accessed 26 October 2022).

[61] S. Muhammad-Bashir, M. Al-Oufi, M. Al-Hakami, M. A. Nadeem, K. Mudiyanselage, H. Idriss, *Sol. Energy* **2020**, *205*, 461–464.

[62] E. Kemppainen, S. Aschbrenner, F. Bao, A. Luxa, C. Schary, R. Bors, S. Janke, I. Dorbandt, B. Stannowski, R. Schlatmann, S. Calnan, *Sustain. Energy Fuels* **2020**, *4*, 4831–4847.

[63] Electrolyser/photovoltaics combinations demonstrated in test fields can be found under https://cordis.europa.eu/article/id/421420-best-electrolyser-photovoltaics-combinations-demonstrated-in-test-fields (accessed 26 October 2022).

[64] The overview of the PECSYS project can be found under https://www.helmholtz-berlin.de/projects/pecsys/ (accessed 26 October 2022).

[65] İ. B. Pehlivan, J. Oscarsson, Z. Qiu, L. Stolt, M. Edoff, T. Edvinsson, *iScience* **2021**, *24*, 101910.

[66] A. Rothschild, H. Dotan, *ACS Energy Lett.* **2017**, *2*, 45.

[67] R. Bhandari, R. R. Shah, *Renewable Energy* **2021**, *177*, 915.

[68] T. Terlouw, C. Bauer, R. McKenna, M. Mazzotti, *Energy Environ. Sci.* **2022**, *15*, 3583.

[69] Levelized cost of electricity renewable energy technologies can be found under https://www.ise.fraunhofer.de/content/dam/ise/en/documents/publications/studies/EN2021_Fraunhofer-ISE_LCOE_Renewable_Energy_Technologies.pdf, **2021** (accessed 26 October 2022).

[70] L.-C. Kin, O. Astakhov, M. Lee, S. Haas, K. Ding, T. Merdzhanova, U. Rau, *Solar RRL* **2022**, *6*, 2100916.

[71] F. F. Abdi, L. Han, A. H. M. Smets, M. Zeman, B. Dam, R. van de Krol, *Nat. Commun.* **2013**, *4*, 2195.

[72] J. H. Kim, Y. Jo, J. H. Kim, J. W. Jang, H. J. Kang, Y. H. Lee, D. S. Kim, Y. Jun, J. S. Lee, *ACS Nano* **2015**, *9*, 11820–11829.

[73] W. J. Chang, K.-H. Lee, H. Ha, K. Jin, G. Kim, S.-T. Hwang, H.-m. Lee, S.-W. Ahn, W. Yoon, H. Seo, J. S. Hong, Y. K. Go, J.-l. Ha, K. T. Nam, *ACS Omega* **2017**, *2*, 1009–1018.

[74] Y. Kageshima, T. Shinagawa, T. Kuwata, J. Nakata, T. Minegishi, K. Takanabe, K. Domen, *Sci. Rep.* **2016**, *6*, 24633.

[75] E. Verlage, S. Hu, R. Liu, R. J. R. Jones, K. Sun, C. Xiang, N. S. Lewis, H. A. Atwater, *Energy Environ. Sci.* **2015**, *8*, 3166–3172.

[76] W.-H. Cheng, M. H. Richter, M. M. May, J. Ohlmann, D. Lackner, F. Dimroth, T. Hannappel, H. A. Atwater, H.-J. Lewerenz, *ACS Energy Lett.* **2018**, *3*, 1795–1800.

[77] S. Rau, S. Vierrath, J. Ohlmann, A. Fallisch, D. Lackner, F. Dimroth, T. Smolinka, *Energy Technol.* **2014**, *2*, 43–53.

[78] G. Peharz, F. Dimroth, U. Wittstadt, *Int. J. Hydrogen Energy* **2007**, *32*, 3248–3252.

[79] S.-H. Hsu, J. Miao, L. Zhang, J. Gao, H. Wang, H. Tao, S.-F. Hung, A. Vasileff, S. Z. Qiao, B. Liu, *Adv. Mater.* **2018**, *30*, 1707261.

[80] B. J. Kim, D. H. Kim, Y.-Y. Lee, H.-W. Shin, G. S. Han, J. S. Hong, K. Mahmood, T. K. Ahn, Y.-C. Joo, K. S. Hong, N.-G. Park, S. Lee, H. S. Jung, *Energy Environ. Sci.* **2015**, *8*, 916–921.

[81] S. Tembhurne, F. Nandjou, S. Haussener, *Nat. Energy* **2019**, *4*, 399–407.

[82] P. Varadhan, H.-C. Fu, Y.-C. Kao, R.-H. Horng, J.-H. He, *Nat. Commun.* **2019**, *10*, 5282.

[83] B. Weng, F. Xu, C. Wang, W. Meng, C. R. Grice, Y. Yan, *Energy Environ. Sci.* **2017**, *10*, 121–128.

[84] J. Luo, D. A. Vermaas, D. Bi, A. Hagfeldt, W. A. Smith, M. Grätzel, *Adv. Energy Mater.* **2016**, *6*, 1600100.

[85] J. Liang, X. Han, Y. Qiu, Q. Fang, B. Zhang, W. Wang, J. Zhang, P. M. Ajayan, J. Lou, *ACS Nano* **2020**, *14*, 5426–5434.

[86] Y. Gao, V. M. Le Corre, A. Gaïtis, M. Neophytou, M. A. Hamid, K. Takanabe, P. M. Beaujuge, *Adv. Mater.* **2016**, *28*, 3366–3373.

[87] S. Esiner, R. E. M. Willems, A. Furlan, W. Li, M. M. Wienk, R. A. J. Janssen, *J. Mater. Chem. A* **2015**, *3*, 23936–23945.

[88] S. H. Kang, M. J. Jeong, Y. K. Eom, I. T. Choi, S. M. Kwon, Y. Yoo, J. Kim, J. Kwon, J. H. Park, H. K. Kim, *Adv. Energy Mater.* **2017**, *7*, 1602117.

[89] S. Y. Chae, S. J. Park, O.-S. Joo, B. K. Min, Y. J. Hwang, *Sol. Energy* **2016**, *135*, 821–826.

[90] H. Park, I. J. Park, M. G. Lee, K. C. Kwon, S.-P. Hong, D. H. Kim, S. A. Lee, T. H. Lee, C. Kim, C. W. Moon, D.-Y. Son, G. H. Jung, H. S. Yang, J. R. Lee, J. Lee, N.-G. Park, S. Y. Kim, J. Y. Kim, H. W. Jang, *ACS Appl. Mater. Interfaces* **2019**, *11*, 33835–33843.

[91] J. Gao, F. Sahli, C. Liu, D. Ren, X. Guo, J. Werner, Q. Jeangros, S. M. Zakeeruddin, C. Ballif, M. Grätzel, J. Luo, *Joule* **2019**, *3*, 2930–2941.

[92] S. K. Karuturi, H. Shen, A. Sharma, F. J. Beck, P. Varadhan, T. Duong, P. R. Narangari, D. Zhang, Y. Wan, J.-H. He, H. H. Tan, C. Jagadish, K. Catchpole, *Adv. Energy Mater.* **2020**, *10*, 2000772.

[93] İ. Bayrak Pehlivan, M. Edoff, L. Stolt, T. Edvinsson, *Energies* **2019**, *12*, 4064.